Single recipient cell tracking of tellurium-labeled extracellular vesicle proteomes (TeLEV) identifies EV-driven immunomodulation

Daniel Bachurski[1,2]*, Rahil Gholamipoorfard[1,3]*, Yong-Jia Bu[4]*, Patrick Hoelker[1,2], Lisa Wessendorf[1,2], Hendrik Jestrabek[1,2], Luca D. Schreurs[1,2], David Stahl[1], Amin Mokhlesi[1,3], Philipp Gödel[1], Felix Gaedke[5], Elias Ranjbari[6] ,Selen Seyhan[7], Ulrike Resch[8], Luisa Marie Schmidt[2,9], Tobias Tertel[10], France Rose[11,12], Cláudio Pinheiro[13,14], Maribel L. Corona[15],Anton von Lom[1,2], Alexander Frederik vom Stein[1,2], Phuong-Hien Nguyen[1,2], Katrin S. Reiners[16], An Hendrix[13,14], Guillaume van Niel[15], Marcus Krüger[2], Katarzyna Bozek[2,11,12], Lydia Meder[17], Per Malmberg[6], Paula Cramer[1], Barbara Eichhorst[1], Martin Peifer[3], Roland T. Ullrich[1,12], Astrid Schauss[5], Christian Pallasch[1,2], Paul J. Bröckelmann[1,18], Ron D. Jachimowicz[1,2,18], Christian Preußer[19], Bernd Giebel[10], Elke Pogge von Strandmann[19], Mark Nitz[4#], Michael Hallek[1,2,12#] and Nima Abedpour[1,3,20#]

These authors contributed equally: Daniel Bachurski, Rahil Gholamipoorfard, Yong-Jia Bu
#These authors jointly supervised this work: Mark Nitz, Michael Hallek, Nima Abedpour

[1] University of Cologne, Faculty of Medicine and University Hospital Cologne, Department I of Internal Medicine, Cologne, Germany
[2] Cologne Excellence Cluster on Cellular Stress Responses in Aging-Associated Diseases (CECAD), University of Cologne, Cologne, Germany
[3] University of Cologne, Faculty of Medicine and University Hospital Cologne, Department of Translational Genomics, Cologne, Germany
[4] Department of Chemistry, University of Toronto, Toronto, ON M5S 3H6, Canada
[5] University of Cologne, Faculty of Mathematics and Natural Sciences, Cologne Excellence Cluster for Aging-Associated Diseases (CECAD), Cologne, Germany
[6] Chalmers University of Technology, Gothenburg, Sweden
[7] Dokuz Eylül University, Izmir, Turkey
[8] University of Vienna, Vienna, Austria
[9] University of Copenhagen, Copenhagen, Denmark
[10] University of Duisburg-Essen, Essen, Germany
[11] Institute for Biomedical Informatics, Faculty of Medicine and University Hospital Cologne, Cologne, Germany
[12] Center for Molecular Medicine Cologne (CMMC), Faculty of Medicine and University Hospital Cologne, Cologne, Germany
[13] Laboratory of Experimental Cancer Research, Department of Human Structure and Repair, Ghent University, Ghent, Belgium
[14] Cancer Research Institute Ghent, Ghent, Belgium
[15] Université Paris Cité, Institute of Psychiatry and Neuroscience of Paris (IPNP), INSERM U1266, van Niel's Team, Paris, France
[16] Institute of Clinical Chemistry and Clinical Pharmacology - Immunology in Translation, University Hospital Bonn, Bonn, Germany
[17] Chair of Experimental Medicine I, Medical Faculty, Friedrich-Alexander-Universität Erlangen-Nürnberg (FAU), Erlangen, Germany
[18] Max Planck Institute for Biology of Ageing, Cologne, Germany
[19] Philipps University of Marburg, Marburg, Germany
[20] Cancer Research Center Cologne-Essen (CCCE), Cologne, Germany

Corresponding author:
Daniel Bachurski
Department I of Internal Medicine, University Hospital Cologne
Kerpener Str. 62, 50937 Cologne, Germany
E-Mail: daniel.bachurski@uk-koeln.de
Phone: +49 221 478 84118

Abstract

Single recipient cell tracking of tellurium-labeled extracellular vesicle proteomes (TeLEV) identifies EV-driven immunomodulation

Extracellular vesicles (EVs) mediate tumor-immune cell communication by carrying protein cargo that can immediately modulate signaling and antigen presentation. Yet mapping the uptake of primary EV proteomes by human immune cells at single-cell resolution has been constrained by a lack of labeling strategies. We show here that TeLEV, a tellurium-based metabolic mass tagging approach that incorporates L-2-tellurienylalanine (TePhe) into EV proteomes, can produce a biologically rare monoisotopic signal, which is detectable by mass cytometry, imaging mass cytometry, and nanoscale SIMS, without perturbing EV morphology, yield, or proteome composition. We applied TeLEV to label primary malignant B-cell-derived EVs (MBC-EVs) from chronic lymphocytic leukemia (CLL) patients and could follow EV uptake by distinct cell populations of peripheral blood mononuclear cells. MBC-EV uptake occurred predominantly in cells of myeloid lineages. In direct control experiments with matched secreted proteins, a machine learning approach identified CD123, CD127, and CD25 as key markers distinguishing primary MBC-EV recipients from matched secreted protein recipient cells. Nanoscale imaging enabled localization of EV-delivered proteins within heterochromatin, whereas Te-labeled secreted proteins accumulated in the cytoplasm of recipient cells. We then generated a pan-immune EV uptake atlas by tracing the uptake of primary and cell-line EVs from nine cell lines and six donors with chronic lymphocytic leukemia into 2,977,094 recipient cells across 43 cell types and subpopulations. We found that the uptake of MBC-EVs by myeloid recipients induced monocyte-derived dendritic-cell polarization characterized by the co-expression of the interleukin-receptor triad (IL-RT: CD123, CD127, CD25) identified above. Time-resolved EV uptake analysis showed a rapid, transient expression of CD123/CD127 followed by CD25, both tightly coupled to MBC-EV uptake by myeloid cells. The intensity of IL-RT expression correlated with that of PD-L1 and BCL-2. Using different STAT degraders to bidirectionally modify the EV-induced STAT5 signal, we observed that MBC-EV uptake and IL-RT, PD-L1, and BCL-2 expression increased with STAT3 degradation and decreased with STAT5 degradation. To investigate the functional consequences of the MBC-EV-induced changes, we showed that MBC-EVs in the presence of IL-2 induced a high-CD25 immune state with low cytotoxic and high B cell proliferation. Taken together, TeLEV represents a novel tool for single-cell tracking of EV proteomes, revealing STAT5-dependent immune remodeling of recipient cells.

Introduction

Tumor-derived extracellular vesicles (EVs) and their protein cargo are potent immune modulators[1–6]. Yet, research on EVs has been limited by tremendous difficulties in identifying the target cells of the EV proteomes and studying their destiny[7–11]. Moreover, functional investigations into the consequences of EV uptake remained limited, as cargo uptake could not be followed at the single-cell level. The central hurdle for this problem was the detection of EVs or the released proteins at single-cell resolution, as most labeling strategies stain material that is not EV, alter the EV biogenesis or function, or conflate EVs with contaminating secreted proteins, thereby disturbing functional studies linking cargo delivery with functional changes of recipient cells[12–15]. An effective solution should provide a minimally disruptive, proteome-sensitive label compatible with various cytometry and imaging methods, and an internal control to distinguish EV-specific from general protein uptake[9,10,16].

To address this problem, we developed TeLEV, a tellurium-based mass tag that labels EV proteomes with minimally perturbing, non-toxic L-2-tellurienylalanine (TePhe) at working concentrations[16,17]. This allowed the creation of matched primary MBC-EV and secreted protein controls based on TePhe, which mimics phenylalanine in both uptake and protein incorporation[18]. The biologically rare monoisotopic tellurium signal enabled cross-platform readout by mass cytometry, imaging mass cytometry, and correlative TEM-nanoSIMS[19–21], allowing detection across multiple platforms and preserving EV morphology and composition.

When applied to MBC-EVs and human peripheral blood mononuclear cells, TeLEV revealed a predominantly myeloid MBC.EV uptake, which induced the coordinated expression of interleukin receptors (CD123, CD127, CD25). EV proteomes upon uptake localized in the heterochromatin of the recipient, while the matched secreted Te-labeled protein control accumulated in the cytoplasm of recipient cells.

To causally interrogate the STAT5-dependence of EV-driven myeloid interleukin receptor programs, we finally paired TeLEV recipient cell analysis with selective degraders of STAT3 and STAT5. For STAT3, we used SD-36, a selective PROTAC that degrades STAT3 and increases STAT5 signaling in dendritic cells, as evidenced by increased pSTAT5[22]. For STAT5, the dual isoform PROTAC AK-2292 degrades STAT5A/B with high selectivity over other STATs[23]. Using both degraders, which bidirectionally modify STAT5 signaling—enhancing it via STAT3 degradation and suppressing it via STAT5 degradation—allowed us to test that EV-driven STAT3/5 programs were necessary to induce the observed myeloid phenotypes in primary recipient cells. We discovered that MBC-EVs activate STAT5 signaling in myeloid cells, orchestrating critical processes such as uptake mechanisms, interleukin receptor programs, and monocytic polarization—highlighting a key role in immune regulation.

Main

Cross-platform recipient cell tracking with matched controls and nanoscale localization

We established TeLEV, a tellurium-based metabolic mass tag in which primary cells or cell lines are cultured with L-2-tellurienylalanine (TePhe), the conditioned medium is fractionated by size-exclusion chromatography, and Te-labeled MBC-EVs (F3–F5) are analyzed alongside matched Te-labeled secreted proteins (F9–F11) from the same secretome (Fig. 1a)[24]. This matched-fractions design allows direct attribution of monoisotopic tellurium to EV-mediated cargo versus freely secreted proteins and enables readout across suspension mass cytometry, imaging mass cytometry, and correlative TEM-nanoSIMS. At single-cell resolution, the approach produced robust Te signals in peripheral blood mononuclear cells (PBMCs) exposed to MBC-EVs for 16 h with negligible background in PBS-HAT controls, and it cleanly distinguished uptake of EV cargo from uptake of matched Te-labeled soluble proteins by high-dimensional analysis of recipient cell phenotypes (Fig. 1b and Extended Data Fig. 1a,b,c). Imaging mass cytometry on sister cultures reproduced heterogeneous recipient-cell intensities with the expected per-pixel sensitivity difference relative to suspension mass cytometry (Fig. 1c)[20]. Correlative TEM-nanoSIMS localized the Te tag derived from Te-labeled primary MBC-EVs predominantly to electron-dense heterochromatin in myeloid recipients[25]. In contrast, the signal from Te-labeled secreted proteins was found to be concentrated in the cytoplasm (Fig. 1d). Together, Figure 1 demonstrates that TeLEV allows for the sensitive, specific tracking of EV proteomes across diverse technologies, from population-level uptake down to nanoscale localization, and to separate it from non-EV mediated protein transfer.

TeLEV preserves EV morphology, abundance, and proteome composition

Because labeling approaches involving modifications to EV-secreting cells could potentially distort the generation of primary EVs or their destiny, we investigated the effects of the TeLEV procedure on EV morphology, abundance, and protein composition[26]. Triplex immunogold TEM for CD9, CD63, and CD81 revealed indistinguishable labeling and preserved cup-shaped morphology in primary Te-labeled MBC-EVs and unlabeled controls. In the absence of uranyl-acetate contrast, primary Te-labeled MBC-EVs remained visible, consistent with intrinsic tellurium-derived contrast that reveals fine ultrastructural features (Fig. 2a). Moreover, nanoparticle tracking analysis (NTA) of MBC-EVs generated from 10 primary CLL donors showed overlapping size distributions. Fractionation by size-exclusion chromatography in 3 donors produced concordant particle and protein profiles, with MBC-EV-enriched fractions peaking at F3–F5 and soluble proteins eluting later (Fig. 2b,c)[27]. Pooled MBC-EV fractions (F3–F5) exhibited no difference in particle counts or modal diameters between TeLEV and control preparations (Fig. 2d,e). Marker distribution and global proteomes were likewise unaffected. Immunoblots placed canonical EV markers (CD81, Flotillin-1, Syntenin) in F3–F5 and excluded GM130 from MBC-EV fractions in both conditions, with total protein enriched in late soluble fractions as expected (Fig. 2f). Shotgun proteomics recapitulated these patterns and revealed no systematic shift with TeLEV. For example, samples clustered by donor rather than labeling status in Pearson-correlation matrices and principal-component analysis, global $\log_2$-intensity distributions, and the numbers of identified proteins were comparable between conditions, and differential testing detected no significantly changed proteins at FDR < 0.05 ($s_0 > 0.1$), including GO-annotated EV proteins (Fig. 2g–m). Together, these data suggested that TeLEV did not measurably perturb MBC-EV morphology, yield, size distribution, or proteome composition across donors, justifying downstream single-cell recipient analyses.

Preferential MBC-EV uptake by myeloid cells

We next mapped primary MBC-EV uptake after 16 h by different immune cells at single-cell resolution (Extended Data Fig. 7). After data cleaning, 785,260 mass cytometry events were integrated to construct a reference PBMC landscape of primary MBC-EV uptake[21]. Unsupervised FlowSOM clustering followed by manual curation identified 43 immune populations and subpopulations, including rare plasmacytoid dendritic cells (pDCs), myeloid dendritic cells (mDCs), γδ T cells, regulatory T cells, and residual low-density neutrophils (Fig. 3a,b). Within this scope, TeLEV quantification revealed MBC-EV-protein uptake across all major cell lineages. However, TeLEV signal was clearly enhanced in myeloid cells, distributed across classical, intermediate, and non-classical monocytes, residual neutrophils, mDCs, and pDCs, but showed lower levels in all lymphoid subsets (Fig. 3c, left and middle)[28]. Cell density distributions showed condition-specific redistributions in myeloid and T-cell compartments relative to vehicle controls, as indicated by shifts in density maxima in the t-SNE space. (Fig. 3c, right). In comparison, matched Te-labeled soluble proteins from the same secretomes were also preferentially taken up by myeloid cell populations and exhibited similar uptake patterns. Te-labeled proteins also resulted in two separate density peaks in classical monocytes and naïve CD4 T cells. Additionally, Te-labeled soluble protein uptake was overall 4.3 times higher (median Te signal all cells primary MBC-EVs 0.5199 vs. matched Te-labeled secreted proteins 2.2486), reflecting the greater abundance of labeled proteins in matched samples (Fig. 2c,f and Fig. 3c, middle). To characterize primary MBC-EV-specific phenotypes, we trained separate random-forest classifiers on cells in the top quintile of Te signal for MBC-EVs or soluble proteins (each relative to control)[29]. We evaluated the EV-to-protein log-ratio

derived from permutation-based feature importance values (Fig. 3d). Interleukin-receptor (IL-R) markers dominated this ratio, CD127 (IL7Rα), CD123 (IL3Rα) (IL-R triad, IL-RT), and CD25 (IL2Rα), with CD25 particularly highlighting TeLEV-positive monocytes and mDCs, including IL-RT positive cells (Extended Data Fig. 2). These findings suggested that primary MBC-EV uptake enhanced specifically IL-R expression in different myeloid recipient cells.

MBC-EVs induce an interleukin-receptor triad and a CD197$^+$ mo-derived DC-like state in myeloid cells

To create a comprehensive immune recipient atlas of EVs from different sources, we investigated 2,977,094 PBMC recipient cells across sixteen conditions (vehicle plus fifteen EVs from nine cell lines and six primary CLL donors, Extended Data Fig. 6). EV input was normalized to the amount of conditioned medium rather than particle count (reported in Supplementary Table 2) due to inaccuracies, methods limitations and detection thresholds of all current EV quantifications methods[9]. A unified t-SNE embedding served as a reference for all comparisons and revealed widespread EV uptake after 16 h (Fig. 4a,b). We modeled cell-type proportions using a Poisson generalized linear mixed model (GLMM) and identified condition-specific frequency shifts in PBMC recipients, mainly affecting the myeloid compartment (Fig. 4c). In PBMC recipients, we observed that certain immune cells, such as IL-R+ and IL-R+/CD197+ monocytes and mDCs, showed an inverse relationship with the frequency of other immune cells, such as non-classical monocytes and neutrophils. This pattern was observed in EV conditions in two of six primary CLL donors (Patients 1 and 4). Additionally, similar cell relationships were found in two cell lines, Ramos (a Burkitt lymphoma) and Su-DHL-4 (a DLBCL line). A high-resolution re-embedding of 276,867 myeloid cells confirmed a recipient cell signature only observed in MBC-EVs but not in malignant non-B cell EVs with enrichment of mDCs, and a CD197$^+$ (CCR7+) monocyte subset with myeloid and DC markers, suggesting a mo-DC differentiation induced by MBC-EVs (Fig. 4d,e). This signature was absent with malignant EVs from non-B cells, but was not elicited by all malignant B cell EVs. Unexpectedly EVs from the CLL lines OSU-CLL and MEC-1 did not reproduce it, indicating dependence on EV source and patient context (Fig. 4f). Across B cell EV sources, the global responses to Ramos and to CLL patient 1 and 4 were most similar, whereas the two CLL cell lines diverged and lacked the MBC signature (Fig. 4f). Particle number did not account for the signature, as CLL patient 1 and Ramos EV preparations contained fewer particles than all other cell lines tested (Supplementary Table 2). In the shared response pattern, myeloid recipient cells increased levels of CD25, CD123, and CD127 (the interleukin receptor triad, IL-RT), with the initial co-expression observed in Patient 1 (Extended Data Fig. 3). Some IL-RT-positive monocytes also showed increased CD197 expression, indicating a transition toward a monocyte-derived dendritic cell-like state. These cells had lower HLA-DR than conventional myeloid dendritic cells, reduced CD14, and lacked CD183 (CXCR3)[30]. Ternary plots showed that MBC-EVs increased CD25 expression of myeloid and lymphoid populations, while some non-B-cell EVs (such as those from HEK293T and HS-5) increased CD127 (Fig. 4g). Two controls confirmed that these effects were specific to EVs, as the feature-importance analysis identified CD25 as a distinguishing marker for EVs compared to soluble proteins (Fig. 3d and Extended Data Fig. 2). Unlabeled EVs from Patient 1 produced the same IL-RT pattern (Extended Data Fig. 3).

Biphasic IL-RT coupled to early myeloid uptake in EV uptake kinetics

We then characterized dynamics by exposing healthy-donor PBMCs to primary MBC-EVs across eleven time points (0–48 h) and jointly analyzing 1,512,100 single cells in a common embedding (Fig. 5a). Tellurium signal became detectable by fifteen minutes, with myeloid cells showing the earliest and strongest uptake (Fig. 5b). Comparing the uptake dynamics of secreted Te-labeled proteins at 2 hours to primary Te-labeled MBC-EV uptake, we observed that MBC-EV uptake was more heterogeneous than the relatively uniform protein uptake in the monocyte compartment (Extended Data Fig. 4). Early cell-composition profiles were stable for roughly the first two hours and then progressively rebalanced after ~4 h, including an increase in CD197$^+$ monocytes consistent with the emergence of a monocyte-derived DC-like state (Fig. 5c). By sixteen hours, uptake patterns converged with those observed in the broader study: monocytes, mDCs, and pDCs dominated primary MBC-EV acquisition, and mDCs/CD197$^+$ IL-R$^+$ monocytes displayed the highest Te levels (Fig. 5d). Quantifying IL-RT trajectories within myeloid lineages revealed a biphasic program tightly coupled to uptake. In monocytes, CD123 and CD127 rose within 15–30 minutes, dipped toward baseline by ~1 hour, and then entered a second phase in which CD127 peaked near eight hours while CD123 continued to increase through 48 hours; CD25 exhibited a delayed induction that lagged CD127 by ~8 hours and remained elevated thereafter (Fig. 5e-f). pDCs and mDCs showed analogous but lineage-specific kinetics, with earlier and higher CD123 in pDCs and more sustained CD25 in mDCs (Fig. 5g). Taken together, primary MBC-EV uptake induced a transient early IL3Rα/IL7Rα rise followed by IL2Rα expression and changes of the immunophenotype of myeloid cells.

Interleukin priming links EV exposure to sustained CD25 induction and heightened IL-2 responsiveness in myeloid cells

To further explore and validate the functional effects of MBC-EVs on the myeloid compartment, we conducted live-cell immunocytochemistry and (phospho)flow cytometry after exposure to MBC-EVs. To confirm our results on a larger scale and to account for heterogeneity and limited patient material, we chose Ramos-EVs as the MBC cell line model because it most closely resembles Pat. 1 EVs in terms of IL-TR expression and monocyte-derived DC induction (Fig. 4). In purified human monocytes, live-cell immunocytochemistry across MBC-EV dose titration showed a dose-dependent increase in CD25; EV-treated monocytes displayed higher viability (low Cytotox NIR signal) and frequent polarized/elongated morphologies, with the highest-CD25 cells typically non-polarized but adjacent to polarized neighbors (Fig. 5h,i). Early flow cytometry at sixteen hours confirmed MBC-EV-dependent increases in CD25 and CD127 across MBC-EV titration, with CD123 decreasing at the highest MBC-EV dose (Fig. 5j). The stimulation by various interleukin combinations revealed MBC-EV-dependent priming in CD14$^+$ purified monocytes. IL-2 plus IL-7 in the presence of MBC-EVs produced pronounced polarization and maximal CD25 by day 7, whereas IL-2 plus IL-3 or IL-3 plus IL-7 did not produce comparable effects; adding IL-2 + IL-3 + IL-7 increased viability and CD25, with stronger responses when combined with EVs (Fig. 5k). Consistent with direct contributions from EV cargo to receptor–ligand landscapes, immunogold TEM detected IL-3, CD123, and CD127 on MBC-EVs (Fig. 5l). Intracellular phospho-flow cytometry linked receptor remodeling to signaling: EV exposure increased pSTAT5 (MBC-EVs vs. Ctrl one-sided Mann–Whitney U test, $p < 0.0001$); a STAT3 degrader further enhanced EV-induced pSTAT5 (Stat3d + MBC-EVs vs. EVs one-sided Mann–Whitney U test, $p < 0.0001$); a STAT5 degrader reduced EV-induced pSTAT5 (Stat5d + MBC-EVs vs. MBC-EVs one-sided Mann–Whitney U test, $p < 0.0001$); and IL-3 alone partially reproduced the MBC-EV-induced pSTAT5 increase (IL3 vs. Ctrl one-sided Mann–Whitney U test, $p < 0.0001$ and MBC-EVs vs. IL3 one-sided Mann–Whitney U test, $p < 0.0001$) (Fig. 5m). In PBMC co-cultures, MBC-EVs induced CD25+ clusters

and enhanced IL-2 responsiveness, while IL-only controls showed the expected down-modulation of CD127 by IL-7 and the unexpected up-modulation by IL-3, underscoring that MBC-EVs reorganize IL-R programs and their downstream signaling properties rather than simply mirroring IL-only behavior (Fig. 5n)[31]. These findings align with the time-resolved biphasic IL-RT and help explain why MBC-EVs preferentially drive a high-CD25 state in myeloid recipients.

STAT5 is required for CD25 induction and polarization and amplifies EV-driven programs

In healthy donor PBMCs imaged for seven days, a STAT5 degrader (AK-2292) abolished MBC-EV-driven monocyte polarization and prevented maximal CD25 induction, whereas anti-CD25 (Basiliximab) had little effect on MBC-EV-induced morphology; neither intervention affected the MBC-EV-associated viability advantage in our in vitro setting (Fig. 5o). In CD14+ purified monocytes, phosphor flow cytometric analysis revealed that STAT3 degradation augmented (Stat3d + MBC-EVs vs. MBC-EVs one-sided Mann–Whitney U test, $p < 0.0001$) and STAT5 degradation attenuated MBC-EV-induced CD25 (Stat5d + MBC-EVs vs. MBC-EVs one-sided Mann–Whitney U test, $p < 0.0001$); STAT5 degradation also lowered CD123 under both control (Stat5d vs. Ctrl one-sided Mann–Whitney U test, $p<0.0001$) and EV conditions (Stat5d + MBC-EVs vs. MBC-EVs one-sided Mann–Whitney U test, $p<0.0001$). IL-3 increased CD123 and CD127 (IL-3 vs. Ctrl, one-sided Mann–Whitney U test, both $p<0.0001$), but not CD25 (IL-3 vs. Ctrl, one-sided Mann–Whitney U test, $p=1$). CD123 and CD127 correlation evident in the controls was diminished in the presence of MBC-EVs (Fig. 5p). These experiments suggest that STAT5 may act as a signaling node for CD25 induction and MBC-EV-dependent morphological polarization of myeloid recipients.

STAT signaling modulates the uptake of MBC-EVs and tunes the IL-RT with checkpoint and survival co-regulation

To assess how STAT signaling influences EV responses, TeLEV tracking was combined with pharmacological degradation of STAT3 or STAT5 (± IL-2), and 3,590,520 PBMCs were profiled across sixteen conditions. Cell-type frequencies remained consistent, allowing direct comparison (Fig. 6a,b). STAT3 degradation globally increased Te-labeled MBC-EV uptake across most lineages, whereas STAT5 degradation decreased it (Fig. 6c,d). The uptake differences were not attributable to generalized activation, as CD69 levels were similar across IL-2 conditions—EV alone, STAT3-degrader + MBC-EVs, and STAT5-degrader + MBC-EVs (Extended Data Fig. 5). In myeloid cells, MBC-EVs increased CD25, CD123, and CD127; STAT5 degradation reduced their expression, and STAT3 degradation further amplified EV-driven IL-R expression (Fig. 6e,f). EV-induced CD127 was less affected by STAT5 loss than CD123, and CD123 was reduced by STAT5 degradation even without MBC-EVs. STAT3 degradation alone did not induce the IL-RT program but enhanced the EV-induced response (Fig. 6g–k). MBC-EVs also increased PD-L1 and BCL-2 in myeloid and dendritic cell subsets, monocytes, mo-derived DCs, mDCs, and pDCs, with these changes heightened by STAT3 degradation and diminished by STAT5 degradation (Fig. 6l,m). At the PBMC level, IL-2 plus MBC-EVs led to high CD25 and lower Ki-67 in cytotoxic lineages, but higher Ki-67 in B cells, even with elevated CD69. STAT3 and STAT5 modulated both EV cargo uptake and interleukin receptor expression, impacting checkpoint and survival markers

Discussion

326 We established TeLEV, a tellurium-based metabolic label that preserved EV morphology and
327 proteome composition. Across a total of 8.9M cells, it traced primary MBC-EV-proteomic
328 transfer into primary single-recipient cells using mass cytometry, imaging mass cytometry, and
329 nanoSIMS[32]. In PBMCs, uptake was myeloid-dominant. MBC-EVs induced a coordinated
330 interleukin receptor triad (CD123, CD127, CD25) with kinetics that aligned with EV uptake.
331 Two design elements guided interpretation. First, TeLEV labeled the MBC-EV proteome while
332 generating matched soluble protein fractions as control conditions, allowing attribution of
333 recipient cell phenotypes to EV-encapsulated proteins rather than co-secreted proteins[9,10,33].
334 Second, labeling did not change EV size distributions, yield, or proteome composition;
335 unlabeled MBC-EVs produced the same recipient-cell patterns.

336 Across nine cell lines and six primary CLL donors, MBC-EVs reproducibly increased CD123,
337 CD127, and CD25 in monocytes and dendritic cells, with source-dependent differences.
338 Importantly, differences in EV count did not explain these MBC-EV-induced interleukin receptor
339 co-expression. MBC-EVs pushed populations toward higher CD25, whereas few non-B
340 sources favored CD127. A subset of triad-positive monocytes acquired CD197 and features of
341 a monocyte-derived dendritic-like state with lower HLA-DR and absent CD183. Unlabeled
342 MBC-EVs reproduced the triad pattern seen with Te-labeled MBC-EVs, supporting EV
343 specificity. Time-resolved analyses showed that myeloid cells rapidly take up MBC-EVs,
344 triggering a rapid but transient increase in CD123 and CD127, followed by a later, longer-
345 lasting increase in CD25[35]. This process was observed across various myeloid cell types and
346 depended on EV dose and the surrounding cytokines[36]. The presence of IL-2 and IL-7, together
347 with MBC-EVs, led to the highest CD25 expression and cell polarization in purified monocytes.
348 In agreement with previous reports, MBC-EVs may deliver IL-3, which initiates STAT5
349 signaling[37–40]. In addition to IL-3, MBC-EVs also expressed CD123 and CD127. Exposure to
350 MBC-EVs boosted pSTAT5, linking receptor changes to signaling activity. Functionally, PBMCs
351 exposed to MBC-EVs and IL-2 became highly activated but did not proliferate as much,
352 especially in cytotoxic cells, while B cells showed increased proliferation. Overall, these results
353 outline a sequence where rapid MBC-EV uptake leads to early receptor priming and later CD25
354 upregulation, resulting in myeloid cells with enhanced survival and PD-L1 expression.

355 Our findings also demonstrate that STAT5 signaling is essential for mediating myeloid cell
356 responses to MBC-EVs. Specifically, loss of STAT5 abolishes the capacity of myeloid cells to
357 maximally upregulate CD25 expression and to acquire characteristic monocyte polarization,
358 indicating that STAT5 is indispensable for the terminal stages of the EV-driven response[41]. In
359 contrast, STAT3 degradation enhances EV uptake and amplifies the IL-RT response in myeloid
360 cells, but this effect depends on the presence of MBC-EVs. This observation suggests that
361 STAT3 functions as a negative regulator of the response, effectively acting as a brake on
362 STAT5 activity[22]. Notably, STAT3 degradation further increases pSTAT5 levels following EV
363 exposure, supporting the role of STAT3 in modulating STAT5 signaling during this process. A
364 novel finding of this study is that the recipient cell's STAT signaling state regulates EV uptake
365 itself, suggesting a feed-forward regulatory loop. A high STAT5/low STAT3 basal state may
366 prime myeloid cells to be more receptive to MBC-EVs, and the EV cargo then further amplifies
367 this state. This is further supported by the reduced CD123 expression observed in the baseline
368 condition exposed to a STAT5 degrader.

369 Pharmacological targeting of STAT3 (leading to increased pSTAT5) or STAT5 (resulting in
370 decreased pSTAT5) enables fine-tuning of both EV- and IL-RT–driven responses[22,23,42].
371 Immune checkpoint and survival markers such as PD-L1 and BCL-2 exhibit parallel regulation:
372 their expression is elevated in response to MBC-EVs, further enhanced by STAT3 loss, and

attenuated by STAT5 loss, mirroring the regulatory patterns seen for CD25 and MBC-EV uptake[22,43,44]. In PBMCs, the combination of IL-2 and MBC-EVs increases CD25 expression, reduces proliferation of cytotoxic lineages, and enhances B cell proliferation compared with IL-2 alone. Collectively, these results indicate that the interplay between EVs and the STAT pathway orchestrates recipient cell adaptation, with STAT5 serving as a requisite driver of late CD25 induction and monocyte polarization, and STAT3 acting as a context-dependent suppressor by regulating STAT5 signaling. This regulatory framework is consistently observed for PD-L1 and BCL-2 across myeloid cell subsets.

Our findings have important implications. First, they help clarify why myeloid remodeling and immune evasion often accompany high EV levels in B-cell malignancies: MBC-EVs appear to shift monocytes toward a CD197^{+}, PD-L1 high, BCL-2 high phenotype that supports cell migration, survival, and engagement of T-cell checkpoints, while also altering IL-2 signaling[44–47]. Second, the comprehensive EV uptake immune atlas developed here supplies quantitative metrics—such as EV uptake, IL-RT marker profiles, and EV-regulated immune profiles—that can be used to assess EV samples or guide experimental designs. Third, the discovery that STAT3 and STAT5 interact to fine-tune cell responses opens the door to experiments combining EV exposure with STAT pathway modulators or defined cytokine mixes to test specific mechanisms, and these strategies can be translated to animal models or patient samples to explore broader applications and therapeutic potential[5,48,49]. Finally, using a minimally disruptive, proteome-sensitive labeling strategy alongside matched soluble protein controls addresses ongoing uncertainty in the field, making it easier to determine whether observed effects are truly caused by MBC-EVs or by other secreted factors[50,51].

Taken together, TeLEV represents a breakthrough technology for high-resolution analysis of EV proteomes at the single-cell level. Using this innovative platform revealed that MBC-EVs actively shape myeloid immune landscapes, orchestrating a sequence of receptor changes that promote survival and immune checkpoint readiness. The STAT3/STAT5 signaling axis emerges as a key regulator, with targeted STAT3 degradation modulating STAT5 activity to finely tune immune responses. By combining nanoscale imaging with large-scale cellular profiling and targeted pathway interventions, TeLEV offers a powerful framework for dissecting EV-driven immunomodulation in both healthy and disease contexts. This technology holds promise for guiding future therapeutic strategies and for controlling EV-mediated effects in B-cell malignancies.

Methods

Primary leukemic samples

Primary CLL cells and PBMCs isolated from the peripheral blood of CLL patients and healthy donor PBMCs were collected at the University Hospital of Cologne after written and informed consent according to the Declaration of Helsinki and with Institutional Review Board approvals at the University of Cologne, no. 13-091 (BioMaSOTA), no. 19-1559 (Buffy Coats), no 21-1317 (SFB1530) and 21-1472. PBMC isolation and CLL cell purification procedures were performed as previously described[52]. CLL cells were freshly isolated to produce cell-conditioned medium. Clinical information relative to patient samples is listed in Supplementary Table 1.

Cell lines and cell culture

HS-5, THP-1, Su-DHL-4, OSU-CLL, MEC-1, Ramos, Jurkat, U-937, HEK293T were cultured in RPMI 1640 (Gibco, #11875093) supplemented with GlutaMAX (Gibco, #61870036), 10%

417 fetal bovine serum (Gibco, #10270106), and 1% penicillin–streptomycin (Gibco, #15140122).
418 All cell lines were tested for Mycoplasma contamination by PCR. All cells were maintained at
419 37°C in a humidified incubator with 5% CO_2. In all mass cytometry experiments, 1 x 10^6 cells
420 were analyzed per condition. For live-cell immunocytochemistry, cultures comprised 25,000
421 monocytes and 50,000 PBMCs. Flow cytometric analyses utilized a total of 100,000 cells per
422 condition.

423 **Stimulation and treatment of recipient cells**

424 Primary purified monocytes or PBMCs were stimulated with 20 ng/mL IL-2 (BioLegend,
425 #589102), 5 ng/mL IL-3 (BioLegend, #578002), and 25 ng/mL IL-7 (BioLegend, #581902)[53–55].
426 STAT3 (SD-36, MedChemExpress, #HY-129602) and STAT5 degraders (AK-2292,
427 MedChemExpress, #HY-148813) were used at 500 nM and compared to DMSO (PanReac
428 AppliChem, #A3672) controls[22,23]. Anti-CD25 antibody (Basiliximab, MedChemExpress, #HY-
429 10885) was used at 10 µg/mL and compared to an isotype control (Invitrogen, #MA5-55090).
430 All stimulation, inhibition, and degradation conditions were simultaneously added with MBC-
431 EVs.

432 **Healthy donor $CD14^+$ monocyte and PBMC isolation**

433 PBMCs were isolated from healthy donor buffy coats. Cells were washed twice in PBS
434 containing 2% FCS and 1 mM EDTA, then counted by flow cytometry. Cell counts were
435 determined by gating on singlets and DAPI-negative events. The necessary number of PBMCs
436 was resuspended to a final concentration of 1×10^8 cells/mL. $CD14^+$ monocytes were purified
437 by magnetic bead positive selection (EasySep Human CD14 Positive Selection Kit II,
438 STEMCELL Technologies, #17818) with an EasySep Magnet (STEMCELL Technologies,
439 #18001) using 100 µL of selection cocktail per 1×10^8 cells. Labeled cells were incubated for
440 6 minutes at room temperature, magnetically separated, and the CD14- fraction was
441 transferred to a new tube. The remaining $CD14^+$ cells were washed twice with 10 mL of buffer,
442 incubated for 3 minutes each time, and the supernatant was decanted. The previously
443 collected $CD14^-$ fraction was again incubated on the magnet for 6 minutes before collecting
444 the final supernatant. Viability was confirmed by DAPI exclusion using flow cytometry. Purified
445 cells were cryopreserved in FBS containing 10% DMSO, cooled at a controlled rate to –80°C,
446 then transferred to -150°C storage for long-term preservation.

447 **EV separation**

448 Primary MBC-EVs were isolated from EDTA-anticoagulated peripheral blood collected by
449 venipuncture from patients with chronic lymphocytic leukemia who presented with leukocytosis
450 ≥ 15,000 leukocytes per mL, and samples were processed immediately (Sarstedt, #003.1524).
451 Leukemic B cells were enriched as untouched cells via immunodensity-based negative
452 selection according to the manufacturer's instructions using the RosetteSep Human B Cell
453 Enrichment Cocktail (STEMCELL Technologies, #15064).

454 For EV production, the primary cells were adjusted to 1.0×10^7 cells/mL, and the cell lines
455 were adjusted to 1.0×10^6 cells/mL, with viability greater than 95% as determined by DAPI
456 xclusion. The cells were washed twice and cultured in serum-free medium for 48 hours.
457 Conditioned supernatants were harvested and clarified by centrifugation at 350 × g for 5
458 minutes at room temperature, followed by 2,000 × g for 10 minutes at 4 °C. The clarified
459 medium was passed through a 0.22 µm PES membrane filter (Filtropur S, Sarstedt,
460 #83.1826.001) after thawing and then concentrated in 10 kDa centrifugal ultrafiltration units
461 (Amicon Ultra-15 10 kDa, Merck Millipore, #UFC901024) to a final volume of 0.5 mL before

being applied to a qEVoriginal 35 nm size-exclusion column (qEVoriginal 35 nm Gen2, Izon, #ICO-35). The concentration step was performed at 4 °C.

Fractions were collected in 1 mL increments once the 0.5 mL load had fully entered the column. Fractions F3–F5 were retained as EV-enriched fractions, and fractions F9–F11 were collected as protein controls. Particle concentrations of the EV-enriched fractions were quantified by nanoparticle tracking analysis as described in the dedicated NTA section, and the samples were then reconcentrated. For functional assays, EV preparations were supplemented with in-house-prepared PBS-HAT as previously reported[56]. All EV samples were stored at −80 °C before use.

TePhe synthesis

125TePhe and 130TePhe (L-2-tellurienylalanine) were synthesized by adapting previously reported methods for the synthesis of TePhe with natural-abundance Te[17,18]. Isotopically enriched Te was sourced from Trace Sciences (Lot 134-1, 92.8% isotopic enrichment for Te-125 and Lot 130Te/9, 99.40% isotopic enrichment for Te-130).

Tellurium-based metabolic labeling of the extracellular vesicle proteome

Immediately after purification, primary CLL cells or cell lines are seeded for media conditioning (see EV separation). 50 µM of the isotopologues Te-125 or Te-130 L-2-tellurienylalanine (TePhe) are added as medium supplements for metabolic labeling of nacent secretomes.

EV assay normalization

Current challenges in EV assay normalization stem from the lack of standardized methods for quantifying EVs across different systems[9,10]. Co-isolated secreted proteins often confound protein yields from EV preparations, and preparations deemed 'pure' typically exhibit very low protein concentrations. Quantification techniques such as nanoparticle tracking analysis (NTA), nanoflow cytometry, and resistance pulse sensing are limited by device-specific detection thresholds, which may exclude smaller EVs (<60 nm) and introduce variability across cell systems. Additionally, TeLEV normalization cannot rely on TePhe incorporation signals, as these are strongly modulated by cellular protein synthesis and secretion rates. To provide a pan-immune EV uptake atlas, we normalized EV input using 25 mL of conditioned medium collected over 48 hours from 25 million cells, thereby facilitating cross-cell-line comparisons. Supplementary Table 2 details EV counts from NTA, volumes, and specifies the input material. We acknowledge that EV input normalization remains an unresolved challenge within current methodological constraints.

Immunoblotting

Cells or MBC-EVs were lysed using RIPA buffer (Cell Signaling Technology, # 9806S). From the cell lysates, 10 µg of protein was loaded per lane. The secretome fractions were adjusted to a cut-off of 10 µg, whereas the EV fractions did not reach this level. The samples were separated on NuPAGE 4-12% Bis-Tris Gel (1.5mm, 15 wells, Invitrogen, # NP0336BOX) under reducing conditions and transferred to a nitrocellulose membrane (Amersham, Protran, # GE10600016). Protein expression was visualized using Revert 700 Total Protein Stain for Western Blot Normalization (LI-COR, # 926-11011). The membranes were blocked for 1 hour at room temperature with Intercept (TBS) Blocking Buffer (LI-COR, #927-60001) and then incubated overnight at 4°C with unlabeled primary antibodies against GM130, Alix, CD19, IgM, HSP90, HSP70, Syntenin-1, and CD81. After washing, the blots were incubated with an IRDye 800CW Donkey anti-Rabbit IgG secondary antibody (1:15,000, LI-COR, #926-32213) for 1

506 hour at room temperature and imaged with a LI-COR Odyssey CLx Imager (Lincoln, Nebraska,
507 USA). To allow re-probing with additional primary antibodies, membranes were stripped using
508 NewBlot Nitro Stripping Buffer (5X, LI-COR, #928-40030) according to the manufacturer's
509 instructions and subsequently re-incubated with alternative primary antibodies.

510 **Nanoparticle tracking analysis**

511 Measurements were performed on a ZetaView PMX-120-12F-R5 (Particle Metrix, Germany)
512 equipped with a 488 nm, 40 mW laser and a CMOS camera. Samples were diluted in PBS to
513 a final volume of 1 mL. Optimal concentrations were determined by pre-testing to achieve 100-
514 300 particles per frame. Each measurement involved one cycle, during which 11 cell positions
515 were scanned at a frame rate of 30 Hz. Instrument settings were: autofocus enabled, camera
516 sensitivity 80.0, shutter 100, and cell temperature 25 °C. Videos were analyzed using ZetaView
517 Software v8.06.01 SP1 with analysis thresholds of maximum particle size 1000 nm, minimum
518 size 10 nm, and minimum brightness 20.

519 **Immunogold transmission electron microscopy**

520 Formvar-coated copper grids (Science Services, Munich) were prepared with 5 µl of undiluted
521 purified EV samples. The grids were incubated with the samples for 20 minutes, blocked for
522 30 minutes (Aurion, #905.001), and washed three times for 2 minutes in PBS containing 0.1%
523 BSA-c (Aurion, #900.099), pH 7.4. Three gold-coupled antibodies or primary unlabeled
524 antibodies (Supplementary Table 3) were diluted 1:25 in PBS with 0.1% BSA-c: CD9, 10 nm
525 (ABCAM, #STN-273562), CD63, 20 nm (ABCAM, #STN-273564), and CD81, 40 nm (ABCAM,
526 #AB273949) combined in one mix. Grids were incubated in drops of antibody solution for 60
527 minutes, washed 6 times for 5 minutes in drops of PBS with 0.1% BSA-c, followed by 3 2-
528 minute washes in PBS. Unlabeled antibodies were detected with a Protein G Immungold
529 detection step at 1:20 dilution (Aurion, #810.133). After washing, grids were fixed for 5 minutes
530 with 1% Glutaraldehyde (Sigma, #G5882-100ML) in PBS and washed three times for 2 minutes
531 in ddH2O. Grids were stained for 4 minutes with 1.5% Uranyl acetate (Agar Scientific,
532 #R1260A) and blotted dry. For each sample, an unstained duplicate was prepared. Images
533 were captured with a Gatan OneView 4K camera on a JEM-2100Plus (Jeol) at 200 kV and
534 analyzed with ImageJ (NIH).

535 **Cytospin and Imaging Mass Cytometry**

536 Fully stained cells (see "Mass cytometric surface and intracellular protein detection" and Fig.
537 1b) were subjected to Cytospin on a Cytospin 4 centrifuge (Epredia, #A78300002) using
538 Shandon EZ Single Cytofunnel assemblies (Epredia, #11972345) and Superfrost Plus glass
539 slides (Epredia, #J1800AMNZ). Optimal cell density was determined by titration to 0.5×10^6
540 cells in 0.5 mL PBS, yielding a single cell layer on the deposition area. After exposure to EVs,
541 the PBMCs were washed and resuspended in PBS, then immediately loaded into the
542 cytofunnel assemblies according to the manufacturer's instructions. Assemblies were mounted
543 with Superfrost Plus slides and centrifuged for 7 min at 800 rpm. Slides were removed and
544 allowed to air dry at room temperature before further processing. IMC of Cytospin preparations
545 was performed on a Hyperion imaging mass cytometer (Standard BioTools), ablating 750 µm
546 x 750 µm representative regions of interest with a laser power of 3 (laser frequency 200 Hz).

547 The imaging mass cytometric images were converted from the mcd format to tiff files, and hot
548 pixels were removed using a previously reported method[57]. We used the pretrained mesmer2
549 model from DeepCell to segment the cells[58]. Namely, images of the nuclear marker DNA and
550 the cytoplasmic marker CD45 were combined into an RGB image (red = DNA, green = CD45,

551 blue = none) and cut into 512x512-pixel patches with a 256-pixel overlap. The Mesmer2 model
552 is called for each patch, yielding nuclear and whole-cell probability maps. The probability maps
553 from all the patches are merged using averaging, and a watershed algorithm is then applied,
554 as in the original DeepCell code. For each detected cell (whole-cell segmentation map), the
555 averaged signal intensity for the marker 125TeLEV is computed and arcsinh-corrected with
556 cofactor 5. For display, aggregates were removed using morphological operations. After otsu
557 thresholding, the connected components are processed with a closing operation with a disk
558 element of radius 1 and with an opening operation with a disk element of radius 2. If the
559 connected component has a radius over 150 pixels, it is considered an aggregate and removed
560 from the detections.

561 **Mass spectrometry sample preparation**

562 Secreted proteins and EV samples collected in PBS were diluted with 1:1 (v:v) 8% SDS in
563 PBS, homogenized by heating for 10 min at 95 °C, and sonicated with a Bioraptor sonicator;
564 the sonication settings were 21 °C water with 10 cycles of 30 on and 30 off. 20 µg protein
565 extract was reduced and alkylated for 10 min at 70 °C using 5 mM TCEP and 15 mM CAA.
566 Protein digestion was performed following the SP3 protocol (Hughes, 2019 #117). In brief, 20
567 µg of both hydrophobic and hydrophilic beads were added to the sample, and the beads were
568 bound by adding 1:1 volume of acetonitrile (ACN). After 8 minutes of incubation time, magnetic
569 beads were immobilized and washed 2x with 70% ethanol and acetonitrile. Proteins were
570 digested with trypsin (substrate:enzyme ratio 100:1) and LysC (substrate:enzyme ratio 200:1)
571 overnight at RT. Samples were acidified to 1% formic acid (FA), then cleaned up using house-
572 made SDB-RPS tips. Desalted peptides were loaded onto Evotips, and separation was
573 performed on an Evosep ONE LC system (Evosep, Denmark) equipped with 8 cm PepSep
574 columns (EvoSep, Denmark) at 45 °C with a gradient length of 30SPD (44 min). Mobile phases
575 were composed of 0.1% FA as solvent A and 0.1% FA in ACN as solvent B. The LC system
576 was coupled to a timsTOF pro 2 using a CaptiveSpray source (both Bruker, Germany).
577 Samples were measured in dia-PASEF mode, with ion mobility calibrated using three ions from
578 the Agilent ESI-Low Tuning Mix, following vendor specifications. The dia-PASEF window
579 ranged in dimension 1/k0 0.7-1.45, with 16x2 Th windows and in dimension m/z from 350 to
580 1250.

581 **LC-MS/MS sample analysis**

582 The mass spectrometry proteomics data have been deposited to the ProteomeXchange
583 Consortium via the PRIDE partner repository with the dataset identifier PXD069581[59]. Acquired
584 spectra were analyzed with DIA-NN (V1.9.1) using library-free search against UniProt Homo
585 Sapiens database (Apr. 2024)[60]. Mass ranges were set according to the settings of the mass
586 spectrometer. Data were further processed using R (v. 4.2.2) with the libraries tidyverse, diann,
587 and data.table, magrittr, FactoMineR, factoextra, and ggplot2, gprofiler, ggplot2. Data input
588 was filtered for unique peptides, q-values < 0.01, and Lib.Q.Value <0.01, PG.Q.Value < 0.01,
589 Global.Q.Value < 0.01, Quantity.Quality > 0.7, Fragment.count >= 4.

590 Further analysis was performed in Perseus (V 1.6.5.0) and InstantClue (V 0.10.10.20211105).
591 Data were filtered to ensure 100% data completeness. Unpaired Student T-tests were
592 performed on s0 = 0.1, FDR < 0.05, and 500 randomizations. Identified GO terms and GMI
593 extracellular vesicle annotation were imported and compared for each group with an unpaired
594 t-test.

595 **Correlative transmission electron microscopy and NanoSIMS analysis of EV recipients**

PBMCs were centrifuged at 350 xg and fixed for 1 h in 2% Glutaraldehyde with 2.5 % Sucrose (Roth, #4621.1) and 3mM CaCl2 (Sigma, #C7902-500G) in 0.1M HEPES buffer (Sigma, #C7902-500G) pH 7,4. The supernatant was removed, and the pellets were mixed with 3% low-melting agarose in 0.2M HEPES buffer, incubated for 10 minutes at 37°C, and hardened at 4°C for 30 minutes. Agarose blocks were cut into pieces of 1 mm^3, washed four times for 15min with 0.1M HEPES buffer, and incubated with 1% Osmium tetroxide (Science Services, #E19190) and 1% Potassium hexacyanoferrate (Sigma, #P8131) for 1 h at 4°C. After 3x5 min washes with 0.1 M Cacodylate buffer (Applichem, #A2140,0100), samples were dehydrated at 4°C using an ascending ethanol series (50%, 70%, 90%, 3x100%) for 15 min each. The sample was incubated in a mixture of 50% ethanol/propylene oxide, then twice in pure propylene oxide for 15 minutes each. Infiltration was performed with a mixture of 50% Epon/propylenoxide and 75% Epon/propylenoxide for 2h each step and with pure Epon (Sigma, #45359-1EA-F) overnight at 4°C. Samples were embedded into TAAB capsules (Agar Scientific, #G3744) and cured for 48 h at 60°C. Ultrathin sections of 70 nm were cut using an ultramicrotome (Leica Microsystems, UC6) and a diamond knife (Diatome, Biel, Switzerland) and picked up using 200 mesh finder Grids without film (Plano, #7FGC200) Sections were stained with 1.5 % uranyl acetate (Agar Scientific, #R1260A) for 15 min at 37°C and 3% Reynolds lead citrate solution made from Lead (II) nitrate (Roth, #HN32.1) and tri-Sodium citrate dehydrate (Roth #4088.3) for 4 min. Images were acquired using a JEM-2100 Plus Transmission Electron Microscope (JEOL) operating at 80kV equipped with a OneView 4K camera (Gatan). Mosaics of regions of interest were acquired using SerialEM [61]. Location of the cell of interest was noted using the finder pattern. After TEM imaging, sections were transferred onto small 5x5 mm silicon wafer pieces (Plano, #G3390). For this, a small drop of water was added to the wafer, and the Grid was placed on the drop with the section facing the wafer. After the water had evaporated, the grid was removed. Wafers were shipped by placing them onto double-sided sticky tape (Tesa, #05338) inside a petry dish. Images of the same cells were acquired using nanoSIMS. Registration of images obtained by electron microscopy and nanoSIMS was done using nuclei as fiducials with the plugin EC-CLEM from the software ICY[62].

Analysis was performed at NanoSIMS Sweden, University of Gothenburg, using a NanoSIMS 50L (CAMECA, Gennevilliers, France). Samples were gold-coated, and a 16 keV Cs^+ primary ion beam of 0.2 pA (D1-5) was used to raster the sample surface. The detectors were tuned to measure 12C2-, 12C14N-, and 130Te- secondary ions. Before imaging, the areas of interest were implanted to achieve a fluence of 5×10^5 $Cs^+.cm^{-2}$ to enhance the ionization yield. Images were acquired on a field size of 10×10 μm^2 with an image resolution of 512×512 pixels and a dwell time of 3 $ms.pixel^{-1}$. 50 planes were accumulated for each sample. NanoSIMS images were visualized and analyzed with the WinImage software (CAMECA, Gennevilliers, France). Sequential image planes were collected, drift corrected, and accumulated to increase ion counts.

Incucyte live cell immunocytochemistry

Live-cell immunocytochemistry on an Incucyte system was performed to quantify surface expression of CD25 and CD127 on primary human cells under standard incubator conditions, with a near-infrared (NIR) cytotoxicity readout. PBMCs were plated at 50,000 cells per well, and purified monocytes were plated at 25,000 cells per well in 100 µL of 0.22 µm-filtered, complete medium in Falcon 96-well black-wall, clear-bottom, tissue culture-treated imaging microplates (Corning Falcon, #353219). Plates were incubated for 1 h at 37 °C and 5% CO_2 before kinetic imaging was initiated. Imaging was conducted on an Incucyte instrument equipped with green, red, and NIR channels using a 20× objective. Phase-contrast and

643 fluorescence images were acquired every 2 h for 48 – 7 days from four non-overlapping fields
644 per well with hardware autofocus enabled. Alexa Fluor 488 was detected in the green channel,
645 phycoerythrin (PE) in the red channel, and Cytotox NIR in the NIR channel. Exposure times
646 were kept within the linear range across the time course using the vendor's recommended
647 presets and were held constant within experiments.

648 For live-cell immunocytochemistry, non-IL-2/IL-7-blocking anti-CD25-Alexa Fluor 488 and anti-
649 CD127-PE were added at 1 µg mL^{-1} each directly to cultures (Supplementary Table 3).
650 Incucyte Cytotox NIR was added at a final concentration of 0.6 µM to report membrane
651 compromise. Image analysis was performed in Incucyte software. Total cell masks were
652 generated from phase-contrast images to estimate object counts, and fluorescence masks
653 were generated in the green and red channels to calculate the fraction of $CD25^+$ and $CD127^+$
654 cells and mean integrated fluorescence per cell at each time point. Local background
655 subtraction was applied for visualization.

656 **Flow cytometry (surface and intracellular phospho-staining)**

657 For flow cytometric analysis, cells were cultured for 16 hours or 2 days in V-bottom 96-well
658 plates (100 µL/well). Cells were first incubated with 0.5 µL TrueStain FcX (BioLegend,
659 #422302) per well, for 15 min at 4°C. Subsequently, surface staining was performed using a
660 pre-titrated antibody cocktail (see Table SX1) for 1 h at 4°C in the dark. Following incubation,
661 cells were washed twice with Cell Staining Buffer (CSB, BioLegend, #420201) and immediately
662 processed for acquisition.

663 For intracellular flow cytometric analysis of phosphoproteins, cells were fixed by adding an
664 equal volume of Fixation Buffer (BioLegend, #420801) directly to the culture medium and
665 incubating for 15 min at 37°C. Fixed cells were washed three times in PBS by centrifugation
666 at 900 × g for 2 min to remove residual fixative. Fixed cells were surface-stained as described
667 above, then permeabilized for intracellular staining.

668 Permeabilization was performed using True-Phos Perm Buffer (BioLegend, #763344) by
669 resuspending cells in 200 µL per well and incubating for at least 1 h at -20°C. Cells were then
670 washed four times with CSB (900 × g, 2 min) and subjected to FcR blocking (as above),
671 followed by overnight staining with an intracellular antibody cocktail at 4°C.

672 After staining, cells were washed twice with CSB and resuspended in the same buffer for flow
673 cytometric acquisition. Data were collected on a Miltenyi MACS Quant X and analyzed using
674 FlowJo software (version 10.10, BD Biosciences).

675 **Antibodies**

676 Antibodies for mass cytometry were either purchased pre-conjugated with heavy metals
677 (Standard BioTools) or conjugated in-house using the Maxpar X8 chelating polymer kit
678 (Standard BioTools) or the Maxpar MCP9 polymer kit (Standard BioTools) according to the
679 manufacturer's instructions. Details on antibody clones, corresponding heavy metal tags, and
680 suppliers are provided in Supplementary Table 3.

681 **Mass cytometric surface and intracellular protein detection**

682 Cells were exposed to EVs in 2 mL deep-well 96-well plates (Eppendorf, #0030502310). After
683 EV incubation, the samples were washed and then incubated in the same plates with IdU at
684 50 µM (Standard BioTools, #201127) for 1 h at 37 °C with 5 % CO_2, followed by two washes
685 before antibody staining. TrueStain FcX Fc-receptor block was added, and the samples were

686 incubated for 15 min at 4 °C. For surface staining, the antibody master mix was added to each
687 well, and the cells were incubated for 45 minutes at 4 °C with intermittent gentle vortexing.
688 They were then washed twice in CSB at 350 × g for 5 minutes at 4 °C (BioLegend, #420201).
689 For intracellular antigen detection, the cells were fixed and permeabilized for 45 min at 4 °C
690 using the FoxP3 fixation/permeabilization buffer set (Invitrogen eBioscience, #00-5523-00),
691 then washed twice in the corresponding permeabilization buffer at 900 × g for 5 min at 4 °C.
692 Fc-receptor block was reapplied for 15 minutes at 4 °C. The intracellular or cytoplasmic
693 antibody master mixes were then added, and the samples were incubated for 45 min at 4 °C
694 with intermittent gentle vortexing, followed by two washes in permeabilization buffer at 900 ×
695 g for 5 min at 4 °C. The cells were fixed in 1.6% methanol-free paraformaldehyde for 10 min
696 at room temperature (ThermoFisher, #28906), then washed and incubated overnight at 4 °C
697 with MaxPar Intercalator-Ir 191/193 at a final concentration of 125 nM prepared in MaxPar
698 fix/perm buffer (Standard BioTools, Intercalator #201192B, Fix and Perm #201067). On the
699 following day, the samples were washed twice in CSB and prepared for acquisition.

700 **Mass cytometric data acquisition**

701 Data were acquired on a Helios mass cytometer (Standard BioTools) with daily instrument
702 quality control and tuning. Manual gating using FCSExpress7 (DeNovo Software) was applied
703 to identify live single cells in the sample convolute based on 140Ce, event length, center, width,
704 DNA (191Ir and 193Ir), and live/dead (103Rh) channels.

705 **Mass cytometry data preprocessing**

706 Signal intensity measurements in mass cytometry (CyTOF) are often influenced by neighboring
707 channels, leading to spillover effects due to inherent technological limitations. These
708 interferences, known as spillover effects, can significantly reduce the accuracy of cell-type
709 identification. To compensate for spillover effects, we use CytoSpill [63], a tool that quantifies and
710 corrects spillover in CyTOF data without requiring single-stained controls. We used the control
711 condition dataset to estimate the spillover matrix with the R package *CytoSpill* (v1.0.1), which
712 was then applied to compensate for the other datasets. Following spillover correction, the
713 single-cell data undergo an inverse hyperbolic sine transformation with a co-factor of 5
714 (arcsinh(x/5)).

715 **FlowSOM clustering of mass cytometry data and cell type annotation**

716 Preprocessed mass cytometry data from multiple experiments were integrated for clustering.
717 The lineage-defining markers 89Y-CD45, 141Pr-CD196, 143Nd-CD123, 144Nd-CD19, 145Nd-
718 CD4, 146Nd-CD8a, 147Sm-CD11c, 148Nd-CD16, 149Sm-CD45RO, 150Nd-CD45RA, 151Eu-
719 CD161, 152Sm-CD194, 153Eu-CD25, 154Sm-CD27, 155Gd-CD57, 156Gd-CD183, 158Gd-
720 CD185, 160Gd-CD28, 161Dy-CD38, 163Dy-CD56, 164Dy-TCRgd, 166Er-CD294, 167Er-
721 CD197, 168Er-CD14, 170Er-CD3, 171Yb-CD20, 172Yb-CD66b, 173Yb-HLA-DR, 174Yb-IgD,
722 176Yb-CD127 were normalized using the 99.9th percentile prior to clustering. Cells were
723 initially grouped into 125 clusters based on lineage marker expressions using the R package
724 FlowSOM (v2.10.0)[64]. These clusters were subsequently manually merged and annotated
725 according to biological relevance, yielding 43 distinct cell populations and subpopulations.

726 **Cell type composition analysis**

727 A generalized linear mixed model (GLMM) with a Poisson outcome[65] was used to model the
728 impact of conditions on cell–type–specific counts, with conditions included as a covariate. The
729 effect of this factor on cell-type composition was estimated through interaction terms with cell

type. Models were fitted using the glmer function from the R package *lme4* (v1.1.37). The fold change is relative to the grand mean and adjusted. Statistical significance was evaluated using the local true sign rate (LTSR), which represents the probability that the estimated direction of effect is correct.

Random Forest analysis

A random forest model was used to evaluate the impact of Te-labeled MBC-EVs and Te-labeled MBC-secreted proteins on recipient cells relative to control cells. For robust comparisons, cells with EV and protein signal levels in the top 20% (highest quintile) were selected. The primary MBC-EV (or Te-labeled protein) and control data were combined, and features were normalized using z-score transformation. This integrated dataset was used to train a random forest classifier with the RandomForestClassifier() function from the Python package scikit-learn (v1.4.0). To address class imbalance, class weights were applied, and hyperparameters were optimized via 5-fold cross-validation. Feature importance was calculated as the average across 10 nested cross-validation runs, with 5 permutations per feature, to estimate each feature's contribution to group differentiation.

Visualization

Visualizations were carried out in R (v.4.3.2) and Python (v.3.10) using scanpy (v.1.11.0)[66], which is a scalable toolkit for analyzing single-cell data. For data visualization, high-dimensional single-cell data were reduced to two dimensions using the nonlinear dimensionality reduction algorithm t-SNE (t-distributed stochastic neighbor embedding)[67]. t-SNE plots were created and visualized using scanpy.

EV-TRACK

We have submitted all relevant data of our experiments to the EV-TRACK knowledge database (EV-TRACK ID: EV250125)[68].

Statistics

All statistical differences were calculated in GraphPad Prism, R, or Python. Statistical tests are indicated in the corresponding figure legends. The immunoblot analyses were repeated twice and showed consistent results. p values below 0.05 were considered statistically significant and are indicated in the figures as follows: *$p < 0.05$, **$p < 0.01$, ***$p < 0.001$, and ****$p < 0.0001$

Conflict of Interest statement:

DB, MH, MN, and YJB are inventors of "Mass-tag labeling of the cellular secretome", as described in PCT patent application PCT/EP2023/062049. The remaining authors declare no conflicts of interest.

Acknowledgments

DB and MH are funded by the German Research Foundation (DFG) SFB1530-455784452 (subprojects B01, Z01, Z02) and the José Carreras Leukemia Foundation (Grant DJCLS 04R/2021). NA is supported by the Cancer Research Center Cologne Essen (CCCE) as well as by the German Research Foundation (DFG) SFB1530-455784452 (subproject Z03) and Project-ID 497777992. DB, DS, RTU, AVL, and HJ are supported by the Mildred Scheel Nachwuchszentrum Grant 70113307 from the German Cancer Aid. RDJ is funded by the

771 German Research Foundation (DFG) FOR5504-496650118 (subproject TP05), JA2439/4-1,
772 and SFB1530-455784452 (subproject C02), by the Ministry for Culture and Science of North
773 Rhine-Westphalia (NW21-062A CANTAR), and by the Behrens-Weise-Foundation (for the
774 Improvement of Human Health). DS was supported by an MD Research Stipend of the Else
775 Kröner Forschungskolleg Clonal Evolution in Cancer, University Hospital Cologne, Cologne,
776 Germany. DB is supported by the Exzellenz Initiieren (E.I.) – Stiftung Kölner Krebsforschung.
777 DB and BE are supported by the German Federal Ministry of Education and Research (BMBF;
778 project 01KU2108) within the ERA PerMed framework. We thank Dr. Dirk Strunk (Paracelsus
779 Medical University) for his scientific insights and guidance. We also thank Dr. Jan van Deun
780 (University of Erlangen-Nuremberg) and Dr. Anna Kashkanova (Max Planck Institute for the
781 Science of Light, Erlangen) for their experimental support. Additionally, we appreciate Dr.
782 Christian Jüngst and Beatrix Martiny (CECAD Imaging Facility, University of Cologne) for their
783 experimental assistance. (Imaging) Mass cytometric data acquisition was carried out by Petra
784 Hofmann (Department I of Internal Medicine) and Marion Müller (Institute of Pathology) at the
785 CyTOF Facility of the Medical Faculty, University of Cologne, supported by the DFG-funded
786 CRC1530 (Project Z02). Immunogold transmission electron microscopy was performed at the
787 CECAD Imaging Facility using a Jeol JEM 2100 Plus, funded by DFG-INST 216/793-1 FUGG.
788 We additionally thank the Regional Computing Center of the University of Cologne for providing
789 computing time on the DFG-funded High Performance Computing system CHEOPS (Funding
790 number: DFG-INST 216/512-1 FUGG) and for support. The NanoSIMS measurements were
791 performed at the NanoSIMS Sweden Facility at the University of Gothenburg, SciLifeLab
792 Swedish infrastructure. Graphical representations were created with BioRender
793 (https://BioRender.com/hlo8aeq).

794 **References**

795 1. Buzas, E. I. The roles of extracellular vesicles in the immune system. *Nat Rev Immunol* **23**, 236–250
796 (2023).
797 2. Kalluri, R. The biology and function of extracellular vesicles in immune response and immunity.
798 *Immunity* **57**, 1752–1768 (2024).
799 3. Alashkar Alhamwe, B. *et al.* BAG6 restricts pancreatic cancer progression by suppressing the
800 release of IL33-presenting extracellular vesicles and the activation of mast cells. *Cell Mol Immunol*
801 **21**, 918–931 (2024).
802 4. van Niel, G., D'Angelo, G. & Raposo, G. Shedding light on the cell biology of extracellular vesicles.
803 *Nat Rev Mol Cell Biol* **19**, 213–228 (2018).
804 5. Kalluri, R. & McAndrews, K. M. The role of extracellular vesicles in cancer. *Cell* **186**, 1610–1626
805 (2023).
806 6. Tran, H. L. *et al.* Extracellular Vesicles for Clinical Diagnostics: From Bulk Measurements to Single-
807 Vesicle Analysis. *ACS Nano* **19**, 28021–28109 (2025).

808 7. Maas, S. L. N. *et al.* Possibilities and limitations of current technologies for quantification of
809 biological extracellular vesicles and synthetic mimics. *Journal of Controlled Release* **200**, 87–96
810 (2015).
811 8. Melling, G. E. Fluorescent labeling of EVs: strengths and limitations. *Sci Rep* (2022).
812 9. Welsh, J. A. *et al.* Minimal information for studies of extracellular vesicles (MISEV2023): From basic
813 to advanced approaches. *J Extracell Vesicles* **13**, e12404 (2024).
814 10. Théry, C. *et al.* Minimal information for studies of extracellular vesicles 2018 (MISEV2018): a
815 position statement of the International Society for Extracellular Vesicles and update of the
816 MISEV2014 guidelines. *J Extracell Vesicles* **7**, 1535750 (2018).
817 11. Seliger, B. & Massa, C. CyTOF as a suitable tool for stratification and monitoring of cancer
818 patients. *Journal of Translational Medicine* **23**, 724 (2025).
819 12. Li, Y.-J., Wu, J.-Y., Wang, J.-M., Hu, X.-B. & Xiang, D.-X. Emerging strategies for labeling and
820 tracking of extracellular vesicles. *J Control Release* **328**, 141–159 (2020).
821 13. Haines, D. S. Confounding lipid dye particles complicate EV labeling studies. *J Extracell*
822 *Vesicles* (2025).
823 14. Tertel, T. *et al.* Imaging flow cytometry challenges the usefulness of classically used
824 extracellular vesicle labeling dyes and qualifies the novel dye Exoria for the labeling of
825 mesenchymal stromal cell-extracellular vesicle preparations. *Cytotherapy* **24**, 619–628 (2022).
826 15. Dehghani, M., Gulvin, S. M., Flax, J. & Gaborski, T. R. Systematic Evaluation of PKH Labelling
827 on Extracellular Vesicle Size by Nanoparticle Tracking Analysis. *Sci Rep* **10**, 9533 (2020).
828 16. Bachurski, D. & Hallek, M. Biological and technical complexities in analyzing extracellular
829 vesicle immune interactions in B-cell malignancies. *FEBS Lett* https://doi.org/10.1002/1873-
830 3468.70102 (2025) doi:10.1002/1873-3468.70102.
831 17. Jia Bu, Y. & Nitz, M. Incorporation of TePhe into Expressed Proteins is Minimally Perturbing.
832 *Chembiochem* **22**, 2449–2456 (2021).
833 18. Bassan, J. *et al.* TePhe, a tellurium-containing phenylalanine mimic, allows monitoring of
834 protein synthesis in vivo with mass cytometry. *Proc Natl Acad Sci U S A* **116**, 8155–8160 (2019).

835 19. Lange, I. Correlative TEM–nanoSIMS for subcellular isotopic localization. *PLOS One* (2021).
836 20. Giesen, C. Imaging mass cytometry by multiplexed metal-tagged antibodies. *Nat Methods*
837 (2014).
838 21. Bendall, S. C. Single-cell mass cytometry of immune system. *Science* (2011).
839 22. Zhou, J. *et al.* STAT5 and STAT3 balance shapes dendritic cell function and tumour immunity.
840 *Nature* **643**, 519–528 (2025).
841 23. Kaneshige, A. *et al.* A selective small-molecule STAT5 PROTAC degrader capable of achieving
842 tumor regression in vivo. *Nat Chem Biol* **19**, 703–711 (2023).
843 24. Monguió-Tortajada, M., Gálvez-Montón, C., Bayes-Genis, A., Roura, S. & Borràs, F. E.
844 Extracellular vesicle isolation methods: rising impact of size-exclusion chromatography. *Cell Mol*
845 *Life Sci* **76**, 2369–2382 (2019).
846 25. Lovrić, J. *et al.* Correlative High-Resolution Imaging of Iron Uptake in Lung Macrophages. *Anal*
847 *Chem* **94**, 12798–12806 (2022).
848 26. Boudna, M. *et al.* Strategies for labelling of exogenous and endogenous extracellular vesicles
849 and their application for in vitro and in vivo functional studies. *Cell Communication and Signaling*
850 **22**, 171 (2024).
851 27. Bachurski, D. *et al.* Extracellular vesicle measurements with nanoparticle tracking analysis -
852 An accuracy and repeatability comparison between NanoSight NS300 and ZetaView. *J Extracell*
853 *Vesicles* **8**, 1596016 (2019).
854 28. Loconte, L. *et al.* Detection of the interactions of tumour derived extracellular vesicles with
855 immune cells is dependent on EV-labelling methods. *J Extracell Vesicles* **12**, e12384 (2023).
856 29. Breiman, L. Random Forests. *Machine Learning* **45**, 5–32 (2001).
857 30. Liu, J., Zhang, X., Cheng, Y. & Cao, X. Dendritic cell migration in inflammation and immunity.
858 *Cell Mol Immunol* **18**, 2461–2471 (2021).
859 31. Carrette, F. & Surh, C. D. IL-7 signaling and CD127 receptor regulation in the control of T cell
860 homeostasis. *Semin Immunol* **24**, 209–217 (2012).

861 32. Willis, L. M. Tellurium-based mass cytometry barcode for live and fixed cells. *Cytometry A*
862 (2018).
863 33. Jeppesen, D. K. *et al.* Reassessment of Exosome Composition. *Cell* **177**, 428-445.e18 (2019).
864 34. Liam-Or, R. *et al.* Cellular uptake and in vivo distribution of mesenchymal-stem-cell-derived
865 extracellular vesicles are protein corona dependent. *Nat. Nanotechnol.* **19**, 846–855 (2024).
866 35. Zhang, B. *et al.* CD127 imprints functional heterogeneity to diversify monocyte responses in
867 inflammatory diseases. *J Exp Med* **219**, e20211191 (2022).
868 36. Jurgielewicz, B. J., Yao, Y. & Stice, S. L. Kinetics and Specificity of HEK293T Extracellular Vesicle
869 Uptake using Imaging Flow Cytometry. *Nanoscale Res Lett* **15**, 170 (2020).
870 37. Lombardo, G. *et al.* Activated Stat5 trafficking Via Endothelial Cell-derived Extracellular
871 Vesicles Controls IL-3 Pro-angiogenic Paracrine Action. *Sci Rep* **6**, 25689 (2016).
872 38. Lopatina, T. *et al.* IL-3 signalling in the tumour microenvironment shapes the immune
873 response via tumour endothelial cell-derived extracellular vesicles. *Pharmacol Res* **179**, 106206
874 (2022).
875 39. Poveda, E. *et al.* Interleukin 18 (IL-18) and IL-3 in Extracellular Vesicles: Biomarkers for
876 Durable Elite Control of HIV-1. *J Infect Dis* **227**, 1381–1385 (2023).
877 40. Bunn, K. E., Giese-Byrne, B. G., Blatt, A. M., Newcomb, D. C. & Pua, H. H. Mouse TH2 cell
878 extracellular vesicles promote eosinophil survival through the surface cytokine cargo IL-3. *Journal*
879 *of Allergy and Clinical Immunology* **156**, 1053–1065 (2025).
880 41. Monaghan, K. L. *et al.* Tetramerization of STAT5 regulates monocyte differentiation and the
881 dextran sulfate sodium-induced colitis in mice. *Front Immunol* **14**, 1117828 (2023).
882 42. Bai, L. *et al.* A Potent and Selective Small-molecule Degrader of STAT3 Achieves Complete
883 Tumor Regression in vivo. *Cancer Cell* **36**, 498-511.e17 (2019).
884 43. Huang, Z.-W. *et al.* STAT5 promotes PD-L1 expression by facilitating histone lactylation to drive
885 immunosuppression in acute myeloid leukemia. *Sig Transduct Target Ther* **8**, 391 (2023).
886 44. Haderk, F. *et al.* Tumor-derived exosomes modulate PD-L1 expression in monocytes. *Sci*
887 *Immunol* **2**, eaah5509 (2017).

888 45. Stahl, D. *et al.* CSF1R+ myeloid-monocytic cells drive CAR-T cell resistance in aggressive B cell
889 lymphoma. *Cancer Cell* **43**, 1476-1494.e10 (2025).
890 46. Grześ, K. M. IL-3/JAK2-STAT5 axis programs human pDC/myeloid responses. *Immunity* (2021).
891 47. Zeng, H. *et al.* Exosomal PD-L1 promotes the formation of an immunosuppressive
892 microenvironment in gastric diffuse large B-cell lymphoma. *Oncol Rep* **49**, 88 (2023).
893 48. Kumar, M. A. *et al.* Extracellular vesicles as tools and targets in therapy for diseases. *Sig*
894 *Transduct Target Ther* **9**, 27 (2024).
895 49. Mentkowski, K. I., Snitzer, J. D., Rusnak, S. & Lang, J. K. Therapeutic Potential of Engineered
896 Extracellular Vesicles. *AAPS J* **20**, 50 (2018).
897 50. Vergauwen, G. *et al.* Confounding factors of ultrafiltration and protein analysis in extracellular
898 vesicle research. *Sci Rep* **7**, 2704 (2017).
899 51. Wallis, R., Mizen, H. & Bishop, C. L. The bright and dark side of extracellular vesicles in the
900 senescence-associated secretory phenotype. *Mechanisms of Ageing and Development* **189**,
901 111263 (2020).
902 52. Vom Stein, A. F. *et al.* LYN kinase programs stromal fibroblasts to facilitate leukemic survival
903 via regulation of c-JUN and THBS1. *Nat Commun* **14**, 1330 (2023).
904 53. Chen, C.-C., Kobayashi, T., Iijima, K., Hsu, F.-C. & Kita, H. IL-33 dysregulates regulatory T (Treg)
905 cells and impairs established immunological tolerance in the lungs. *J Allergy Clin Immunol* **140**,
906 1351-1363.e7 (2017).
907 54. Peng, X., Zhao, M., Gao, L., Sen, R. & MacGlashan, D. Identifying regulatory pathways of
908 spleen tyrosine kinase expression in human basophils. *Journal of Allergy and Clinical Immunology*
909 **145**, 947–957 (2020).
910 55. Singh, K. *et al.* IL-7–mediated expansion of autologous lymphocytes increases CD8+ VLA-4
911 expression and accumulation in glioblastoma models. *J Clin Invest* **135**, e181471.
912 56. Görgens, A. *et al.* Identification of storage conditions stabilizing extracellular vesicles
913 preparations. *J Extracell Vesicles* **11**, e12238 (2022).

914 57. Xiao, X. *et al.* Dice-XMBD: Deep Learning-Based Cell Segmentation for Imaging Mass
915 Cytometry. *Front. Genet.* **12**, (2021).
916 58. Greenwald, N. F. *et al.* Whole-cell segmentation of tissue images with human-level
917 performance using large-scale data annotation and deep learning. *Nat Biotechnol* **40**, 555–565
918 (2022).
919 59. Perez-Riverol, Y. *et al.* The PRIDE database at 20 years: 2025 update. *Nucleic Acids Research*
920 **53**, D543–D553 (2025).
921 60. Demichev, V., Messner, C. B., Vernardis, S. I., Lilley, K. S. & Ralser, M. DIA-NN: neural networks
922 and interference correction enable deep proteome coverage in high throughput. *Nat Methods* **17**,
923 41–44 (2020).
924 61. Mastronarde, D. N. Automated electron microscope tomography using robust prediction of
925 specimen movements. *Journal of Structural Biology* **152**, 36–51 (2005).
926 62. Paul-Gilloteaux, P. *et al.* eC-CLEM: flexible multidimensional registration software for
927 correlative microscopies. *Nat Methods* **14**, 102–103 (2017).
928 63. Chevrier, S. *et al.* Compensation of Signal Spillover in Suspension and Imaging Mass
929 Cytometry. *Cell Syst* **6**, 612-620.e5 (2018).
930 64. Van Gassen, S. *et al.* FlowSOM: Using self-organizing maps for visualization and interpretation
931 of cytometry data. *Cytometry A* **87**, 636–645 (2015).
932 65. Yoshida, M. *et al.* Local and systemic responses to SARS-CoV-2 infection in children and
933 adults. *Nature* **602**, 321–327 (2022).
934 66. Wolf, F. A., Angerer, P. & Theis, F. J. SCANPY: large-scale single-cell gene expression data
935 analysis. *Genome Biology* **19**, 15 (2018).
936 67. Maaten, L. van der & Hinton, G. Visualizing Data using t-SNE. *Journal of Machine Learning*
937 *Research* **9**, 2579–2605 (2008).
938 68. EV-TRACK Consortium *et al.* EV-TRACK: transparent reporting and centralizing knowledge in
939 extracellular vesicle research. *Nat Methods* **14**, 228–232 (2017).

940 **Figure legends**

941 **Fig.1 Single-cell tracking of tellurium-labeled EV proteomes.**

942 a, Schematic of the TeLEV (tellurium-based labeling of the extracellular vesicle proteome)
943 mass-tag labeling workflow yielding Te-labeled MBC-EVs. Primary chronic lymphocytic
944 leukemia cells or cell lines were cultured for 48 h in chemically defined, serum-free medium
945 supplemented with 50 μM L-2-tellurienylalanine (TePhe). Conditioned medium was collected,
946 0.22 μm filtered, concentrated by 10 kDa ultrafiltration (Amicon 10 kDa RC), and fractionated
947 to separate EVs from soluble secreted proteins by size-exclusion chromatography (35 nm
948 resin; IZON qEV original 2).

949 b, Mass cytometry of PBMC recipient cells showing a two-dimensional t-SNE embedding
950 colored by the TeLEV signal originating from primary CLL donors. Columns show PBS-HAT
951 vehicle control (left), CLL-derived MBC-EVs (middle), and Te-labeled soluble proteins (right).
952 *HAT* denotes HEPES, human albumin, and trehalose. Data were acquired on a Helios mass
953 cytometer. Primary MBC-EVs and secreted proteins shown in Fig. 1 were isolated from 25 mL
954 of cell-conditioned medium (from 25M primary CLL cells over 48 hours), resulting in 1.4 x 10^{10}
955 MBC-EVs used per EV condition.

956 c, Imaging mass cytometry of PBMC recipients exposed to PBS–HAT control, CLL-derived
957 MBC-EVs, or Te-labeled secreted proteins. Representative fields are shown (acquired on a
958 Hyperion imaging mass cytometer). Scale bar, 200 μm.

959 d, Correlative ultrastructural and isotopic mapping of PBMC recipients. Transmission electron
960 microscopy (TEM) on 70 nm sections was followed by nanoSIMS of the same regions of the
961 same grids (NanoSIMS 50L; CAMECA, Gennevilliers, France) to detect tellurium enrichment.
962 Arrows indicate TeLEV signal (heat-map overlay) localized predominantly in heterochromatin
963 of myeloid recipients after Te-EV exposure (middle) and in the cytoplasm after exposure to Te-
964 labeled soluble proteins (right). Scale bar, 2 μm.

965

966 **Fig.2 TeLEV does not perturb EV proteomes.**

967 a, Triplex immunogold labeling of tetraspanins on MBC-EVs. Primary CLL-derived MBC-EVs
968 and unlabeled control MBC-EVs were stained with anti-tetraspanin antibodies coupled to
969 distinct gold sizes: CD9 (10 nm), CD63 (20 nm), and CD81 (40 nm), with and without uranyl-
970 acetate contrasting. Representative micrographs are shown. Scale bars, 100 nm (100,000×)
971 and 200 nm (30,000×). MBC-EVs and secreted proteins shown in Fig. 2 were isolated from 50
972 mL of cell-conditioned medium (from 50M primary CLL cells over 48 hours).

973 b, Particle sizing of purified primary MBC-EVs. Nanoparticle tracking analysis (NTA) reported
974 particle size distributions. Statistical significance was evaluated using the Kolmogorov-Smirnov
975 test. Data are represented as mean + SEM.

976 c, Size-exclusion chromatography (SEC) fractionation of conditioned medium. 1 mL fractions
977 were collected and analyzed by NTA (particle counts) and BCA (protein). F1–F2, void volume;
978 F3–F5, EV-enriched (MBC-EVs) fractions; F9–F11, secreted-protein fractions. SEC used 35
979 nm IZON resin following 10 kDa ultrafiltration. Data are represented as mean ± SEM.

980 d, NTA particle counts for pooled primary MBC-EV fractions (F3–F5). No significant changes
981 were identified based on Wilcoxon matched pairs signed rank test (p value = 0.8457).

982 e, NTA particle diameters for pooled primary MBC-EV fractions (F3–F5). No significant
983 changes were identified based on Wilcoxon matched pairs signed rank test (p value = 0.3008).

984 f, Immunoblot analysis of SEC fractions from primary-leukemic donors. Fractions were
985 concentrated and loaded at equal volumes; total-protein staining shows higher abundance in
986 soluble-protein fractions. EV and non-EV markers are shown for TeLEV and control conditions.
987 To avoid overloading of the gel, a 10 µg cut-off of protein fractions was chosen, which was not
988 exceeded by the EV fractions.

989 g, Proteomics comparison of isolated primary MBC-EVs and soluble secreted proteins with
990 and without TeLEV treatment. Heatmap shows $\log_2$ intensity values for selected marker
991 proteins across conditions (n = 3 paired CLL donors).

992 h, Pearson correlation of protein intensities from isolated primary MBC-EVs (left) and secreted
993 proteins (right), showing no clustering based on TeLEV treatment.

994 i, Bar plots of $\log_2$ intensities from isolated primary MBC-EVs (left) and secreted proteins (right)
995 in control and TeLEV-treated samples.

996 j, Mean number of total identified proteins (left) and EV proteins (right) in control and TeLEV-
997 treated samples of isolated primary MBC-EVs and secreted proteins. Data are represented as
998 mean ± SEM.

999 k, Principal component analysis of isolated primary MBC-EVs (left) and secreted proteins
1000 (right), showing no grouping based on TeLEV treatment.

1001 l, Volcano plot showing differences of $\log_2$ intensities between TeLEV-treated and control
1002 samples in isolated primary MBC-EVs. No significantly abundant proteins were identified
1003 (Student's t test: FDR < 0.05, s0 > 0.1). GO term-annotated "extracellular vesicle"
1004 (GO:1903561) proteins are marked in light blue.

1005 m, Boxplot of mean $\log_2$ intensities for control and TeLEV-treated samples of isolated primary
1006 MBC-EVs and secreted proteins based on the GO term "vesicle membrane" (GO:1903561)
1007 and MGI GO EV annotation (GO:1903561). Data are represented as mean ± SEM. No
1008 significantly changed proteins were identified based on unpaired t-test (*p < 0.05, **p < 0.01,
1009 ***p < 0.001).

1010

1011 **Fig.3 Single-cell mapping of PBMC uptake of Te-labeled EVs and soluble proteins**
1012 **secreted by CLL cells.**

1013 a, t-SNE projection of PBMC recipient cells (758,260 cells in total) of PBS-HAT control (329,774
1014 cells), primary MBC-EVs (226,157cells), and matched Te-labeled secreted proteins (229,329
1015 cells), coloured according to cell type. Numerical annotations indicate the relative proportions
1016 of each cell lineage. Primary MBC-EVs and secreted proteins shown in Fig. 3 were isolated
1017 from 25 mL of cell-conditioned medium (from 25M primary CLL cells over 48 hours), resulting
1018 in 1.4 x 10^{10} MBC-EVs used per EV condition.

1019 b, Dot plot depicting the expression of selected markers across major cell types and their
1020 subtypes from three conditions, PBS-HAT control, primary Te-labeled MBC-EVs, and matched
1021 Te-labeled secreted proteins. Dot size corresponds to the proportion of cells expressing each
1022 marker within a given cell type, and color intensity indicates the mean expression level.

1023 c, Comparison of TeLEV signal distribution across major cell types and their subtypes in each
1024 indicated condition, with colors representing the average TeLEV signal level in each population.
1025 Bars above the plots show the relative proportions of each population in the corresponding
1026 condition (left). White lines denote the median, edges the IQR, and whiskers either 1.5 × IQR
1027 or minima/maxima (if no point exceeded 1.5 × IQR; minima/maxima are indicated by the violin
1028 plot range). t-SNE projection of cells for each condition showing TeLEV signal (middle). Two-
1029 dimensional density distributions of cells in t-SNE embedding space, stratified by conditions
1030 (right).

1031 d, Feature importance of EV-to-protein log ratios as determined by the random forest classifier,
1032 where higher positive values indicate stronger discriminative power in primary MBC-EVs
1033 compared to matched Te-labeled secreted proteins.

1034

1035 **Fig.4 Pan-immune single-cell atlas identifies an interleukin-receptor triad induced by**
1036 **B-cell malignant EVs.**

1037 a, t-SNE projection of PBMC recipient cells across 16 conditions (PBS-HAT control plus 15 EV
1038 sources, in total 2,977,094 cells), colored according to cell type. Numerical annotations
1039 indicate the relative proportions of each cell lineage. EVs shown in Fig. 4 were isolated from
1040 25 mL of cell-conditioned medium (from 25M primary CLL cells or cell lines over 48 hours).
1041 The EV uptake conditions were normalized according to the input volume of cell-conditioned
1042 media (25 mL, 25M cells over 48 hours), and EV counts and buffer volumes are reported in
1043 Supplementary Table 2.

1044 b, t-SNE projection of PBMC recipients across 16 conditions showing TeLEV signal.

1045 c, Fold changes in cell type proportions across conditions, estimated using a Poisson
1046 generalized linear mixed model that accounts for confounding factors (Methods). Dot size
1047 represents the probability of change, measured as the local true sign rate (LTSR).

1048 d, t-SNE projection of myeloid cells across 16 conditions (276, 867 cells), colored according to
1049 subtypes.

1050 e, t-SNE plots showing expression of monocytic and DC lineage markers and interleukin
1051 receptors on myeloid cells.

1052 f, Two-dimensional density distributions of myeloid cells in t-SNE embedding space, stratified
1053 by conditions.

1054 g, A cell type–color–coded ternary plot depicting expression levels of CD25, CD123, and
1055 CD127. Circle size reflects the average TeLEV signal level within each cell type. Colors
1056 correspond to those in the legend shown in (a)

1057

1058 **Fig. 5 Temporal dynamics and functional consequence of the interleukin receptor triad.**

1059 a, t-SNE projection of PBMC recipient cells across 11 time points (0-48h, in total 1,512,100
1060 cells) of EV uptake, colored according to cell type. Numerical annotations indicate the relative
1061 proportions of each cell lineage. Primary MBC-EVs and secreted proteins shown in Fig. 5a-g
1062 were isolated from 4,2 mL of cell-conditioned medium (from 4.2M primary CLL cells over 48
1063 hours), resulting in 2.7 x 10^9 EVs used per time point condition.

b, t-SNE plots showing TeLEV signal, CD25, CD127, and CD123 expression at selected time points (columns).

c, Stacked bar plot depicting changes in cell type composition over 48h. Colors correspond to those in the legend shown in (a).

d, Comparison of TeLEV signal distribution across major cell types and their subtypes at 16 h, with colors representing the average TeLEV signal level in each population. Bars above the plots show the relative proportions of each population. White lines denote the median, edges the IQR, and whiskers either 1.5 × IQR or minima/maxima (if no point exceeded 1.5 × IQR; minima/maxima are indicated by the violin plot range).

e, Comparison of TeLEV signal, CD25, CD123, and CD127 distributions within the Monocyte population (including Non-classical Monocytes, Intermediate Monocytes, Classical Monocytes, IL2R/IL7R^{+} Monocytes, and CD197^{+} IL2R/IL7R^{+} Monocytes) over 48 h. Statistical significance across all time points for each marker was evaluated using the Kruskal-Wallis test. Pairwise comparisons between 00 h and 00 h 15 min were performed using a one-sided Mann–Whitney U test. *p-values* < 0.05 were considered significant and are indicated in the figures as follows: *$p < 0.05$, **$p < 0.01$, ***$p < 0.001$, and ****$p < 0.0001$.

f, Line plots depicting the mean expression levels of TeLEV signal, CD25, CD123, and CD127 within the Monocytes during the first 2 hours of EV uptake. Error bars represent mean ± SEM.

g, The same analysis as in (e) for mDCs (left) and pDCs (right).

h, Live-cell immunocytochemistry of purified monocytes exposed to increasing doses of Ramos-derived EVs. Representative frames from day 2 and day 7 are shown. CD25 (Alexa Fluor 488; green) and Cytotox NIR (blue; loss of membrane integrity) are displayed after automated single-cell segmentation (Incucyte built-in). Cells were seeded at 25,000 per well and imaged every 2 h for 7 days using an Incucyte SX5 (20× objective). Scale bar, 200 µm. EVs and secreted proteins shown in Fig. 5h-p were isolated from 1.5 mL of cell-conditioned medium (from 1.5M Ramos cells over 48 hours), resulting in 9 x 10^{8} EVs used per EV condition (3X condition, Fig. 6h,i,j).

i, Single-cell quantification of CD25 (Alexa Fluor 488) fluorescence over 7 days corresponding to (h). Values are unnormalized arbitrary units; data shown as mean ± SEM; n = 4 fields of view.

j, Flow cytometric contour plots of purified monocytes after 16 h of EV exposure across a dose titration (see Figure legend Fig. 6i). CD25 (APC), CD123 (PE), and CD127 (FITC) were measured on a Miltenyi MACSQuant X with compensation using BioLegend compensation beads. DAPI was used as a surface-flow viability dye.

k, Live-cell immunocytochemistry of EV-exposed monocytes stimulated with cytokines. Representative images from day 7 are shown for IL-2 (20 ng mL^{-1}), IL-3 (5 ng mL^{-1}), or, IL-7 (25 ng mL^{-1}), or IL-2 + IL-3, IL-2 + IL-7, IL-3 + IL-7, or IL-2 + IL-3 + IL-7 in RPMI with serum. CD25 (Alexa Fluor 488; green) and Cytotox NIR (blue) are shown after automated segmentation and background subtraction. Imaging on Incucyte SX5 (20×, 2 h intervals). Scale bar, 200 µm.

l, Immunogold transmission electron microscopy of Ramos-EVs labeled for IL-3, CD123, and CD127 alongside an isotype control. Scale bar, 100 nm.

m, Intracellular phospho-flow cytometry of purified monocytes incubated with EVs, showing total STAT5 (Alexa Fluor 488), total STAT3 (PE), pSTAT5 (PE-Cy7), and pSTAT3 (BV421). EV exposure was terminated by immediate formaldehyde fixation after 16 h prior to staining. Cleaved caspase was included as an apoptosis marker. Acquisition on a Miltenyi MACSQuant X with bead-based compensation of all markers.

n, Live-cell immunocytochemistry of EV-exposed healthy-donor PBMCs stimulated for 2 days with IL-2 (20 ng mL^{-1}), IL-3 (5 ng mL^{-1}), or IL-7 (25 ng mL^{-1}) in RPMI with serum. Representative images are shown (Incucyte SX5, 20×, 2 h intervals). Scale bar, 200 μm.

o, Live-cell immunocytochemistry of EV-exposed healthy-donor PBMCs treated for 7 days with a STAT5 degrader (AK-2292) or anti-CD25 (Basiliximab), compared with DMSO and isotype controls. CD25 (Alexa Fluor 488; green), CD127 (PE; red), and Cytotox NIR (blue) are shown after automated segmentation and background subtraction. Cells were seeded at 50,000 per well and imaged on an Incucyte SX5 (20×, every 2 h). Scale bar, 200 μm.

p, Flow-cytometric contour plots of healthy-donor PBMCs after 48 h of EV exposure across a dose titration (1× = 3×10^8 EVs per 10^5 cells), showing CD25 (APC), CD123 (PE), and CD127 (FITC). Acquisition and compensation as in (m).

Fig.6 EV-driven immunomodulation by STAT5-regulated interleukin receptor triad.

a, t-SNE projection of 16 conditions (in total 3,590,520 cells) coloured according to cell type. Numerical annotations indicate the relative proportions of each cell lineage. MBC-EVs shown in Fig. 6 were isolated from 8 mL of cell-conditioned medium (from 8M Ramos cells over 48 hours), resulting in 5 x 10^9 EVs used per EV condition.

b, Stacked bar plot depicting changes in cell type composition. Colors correspond to those in the legend shown in (a).

c, Comparison of TeLEV signal distribution across major cell types and their subtypes. Shown are EVs (217,211 cells), STAT5d + EVs (226,884 cells), and STAT3d + EVs (206,018 cells) conditions, with colors representing the average TeLEV signal level in each population. Bars above the plots show the relative proportions of each population in the corresponding condition (left). White lines denote the median, edges the IQR and whiskers either 1.5 × IQR or minima/maxima (if no point exceeded 1.5 × IQR; minima/maxima are indicated by the violin plot range). t-SNE projection of cells for each condition showing TeLEV signal (middle). Two-dimensional density distributions of cells in t-SNE embedding space, stratified by conditions (right).

d, Comparison of TeLEV signal distribution across three conditions shown in (c). Pairwise comparisons were performed using a two-sided Mann–Whitney U test. ****$p < 0.0001$.

e, t-SNE projection of myeloid population of 16 conditions (865,413 cells), colored according to subtypes.

f, t-SNE plots showing expression of monocytic and DC lineage markers and interleukin receptors on myeloid cells.

g-k, t-SNE plots showing CD25, CD127, CD123, BCL-2, and PD-L1 expressions across the indicated conditions.

l, Comparison of PD-L1 expression distribution across the indicated conditions in Monocytes, mo-derived DCs, mDCs, and pDCs. For each cell type, statistical significance across all conditions was evaluated using the Kruskal-Wallis test.****$p < 0.0001$.

m, Same as in (l) for BCL-2.

n-p, Comparison of CD25 (n), Ki-67 (o), and CD69 (p) expression distributions across major cell types and their subtypes, with colors representing the average respective marker expression level in each population. Shown are IL-2 (238,611 cells) and IL-2 + EVs (207,300 cells) conditions.

Extended Data legends

Extended Data Fig. 1 High-dimensional profiling of MBC-EV recipients

a-c, t-SNE plots showing selected marker expressions for the three conditions. PBS-HAT control, primary Te-labeled MBC-EVs, and matched Te-labeled secreted proteins.

Extended Data Fig. 2 Characterization of Te-labeled CLL-derived EVs and secreted proteins across immune cell populations.

a, Dot plot depicting the expression of selected markers across major cell types and their subtypes for three conditions: PBS-HAT control (top, 329,774 cells), primary Te-labeled MBC-EVs (middle, 226,157 cells), and Te-labeled secreted proteins (bottom, 229,329 cells). Dot size corresponds to the proportion of cells expressing each marker within a given cell type, and color intensity indicates the mean expression level.

b, Feature importance of surface markers for distinguishing the primary MBC-EV from control data, as determined by a random forest classifier (left). The same analysis as in (b) is shown for matched Te-labeled secreted proteins (right).

c, TeLEV signal histograms for primary MBC-EVs (top) and matched secreted proteins (bottom). The dashed lines indicate the 80th percentile cut-off.

d, t-SNE plots showing CD25, CD127, and CD123 expressions for the three conditions.

Extended Data Fig. 3 Comparison of EV uptake from primary and cell line-derived EV sources.

EV uptake

a, t-SNE projection of PBMC recipient cells for 16 conditions (PBS-HAT control plus 15 EV sources) showing TeLEV signal.

b, Two-dimensional density distributions of cells in t-SNE embedding space, stratified by conditions.

c, t-SNE projection of PBMC recipients of PBS-HAT control (200,468 cells), unlabeled control EVs (200,629 cells), and Te-labeled MBC-EVs (191,964 cells) from primary CLL cells coloured according to cell type (column 1). Two-dimensional density distributions of cells in t-SNE embedding space, stratified by conditions (column 2). t-SNE plots showing CD25, CD123, and CD127 expression, and TeLEV signal (columns 3-6).

d, As in c showing the myeloid compartment. Shown are PBS-HAT control (17,445 cells), unlabeled control MBC-EVs (19,003 cells), and Te-labeled MBC-EVs (15,300 cells) from primary CLL cells.

Extended Data Fig. 4 Time-resolved uptake of Te-labeled primary MBC-EVs and MBC-secreted proteins.

a, t-SNE projection of PBMC recipient cells showing uptake dynamics across 11 time points for primary Te-labeled MBC-EVs and 11 time points for matched secreted proteins (in total 2,900,351 cells), coloured according to cell type. Numerical annotations indicate the relative proportions of each cell lineage.

b, t-SNE plots showing TeLEV expressions for 11 time points of MBC-EV uptake.

c, t-SNE plots showing TeLEV expressions for 11 time points of Te-labeled secreted proteins uptake.

d, t-SNE plots showing TeLEV expression for primary MBC-EV uptake (left, 1,512,100 cells) and matched Te-labeled secreted protein uptake (right, 1,388,251 cells) across concatenated time points.

e, Two-dimensional density distributions of cells in t-SNE space for MBC-EV (left) and matched secreted protein conditions (right).

f, Fold changes in cell type proportions across 11 time points of EV uptake, estimated using a Poisson generalized linear mixed model. Dot size represents the probability of change, measured as the local true sign rate (LTSR).

Extended Data Fig. 5 Global immune cell expression of the interleukin receptor triad.

a, t-SNE projection of cells showing CD69 expression. Shown are MBC-EVs (217,211 cells), STAT5d + MBC-EVs (226,884 cells), and STAT3d + MBC-EVs (206,018 cells) conditions.

b, A cell type–color–coded ternary plot depicting expression levels of CD25, CD123, and CD127. Circle size reflects the average TeLEV level within each cell type.

c, t-SNE projection of the non-myeloid population of 16 conditions (2,725,107 cells), colored according to cell types. Numerical annotations indicate the relative proportions of each cell lineage.

d-f, t-SNE plots showing CD25 (d), CD123 (e), and CD127 (f) expressions on the non-myeloid population across the indicated conditions.

g-i, Comparison of CD25 (g), CD123 (h), and CD127 (i) expression distributions across the indicated conditions in Monocytes, mo-derived DCs, mDCs, and pDCs. For each cell type, statistical significance across all conditions was evaluated using the Kruskal-Wallis test. ****$p < 0.0001$. White lines denote the median, edges the IQR, and whiskers either 1.5 × IQR or minima/maxima (if no point exceeded 1.5 × IQR; minima/maxima are indicated by the violin plot range).

Extended Data Fig. 6 Pan-immune cell atlas of EV uptake from cell lines and primary MBC-EVs

t-SNE projection of major cell types per condition. Shown are cell type overlays, two-dimensional density distributions in t-SNE space, and overlays of selected marker expressions.

Extended Data Fig. 7 Immune recipient cell mapping of primary MBC-EV and MBC-secreted protein uptake

t-SNE projection of major cell types per condition. Shown are cell type overlays, two-dimensional density distributions in t-SNE space, and overlays of selected marker expressions of primary Te-labeled MBC-EV and matched secreted protein uptake.

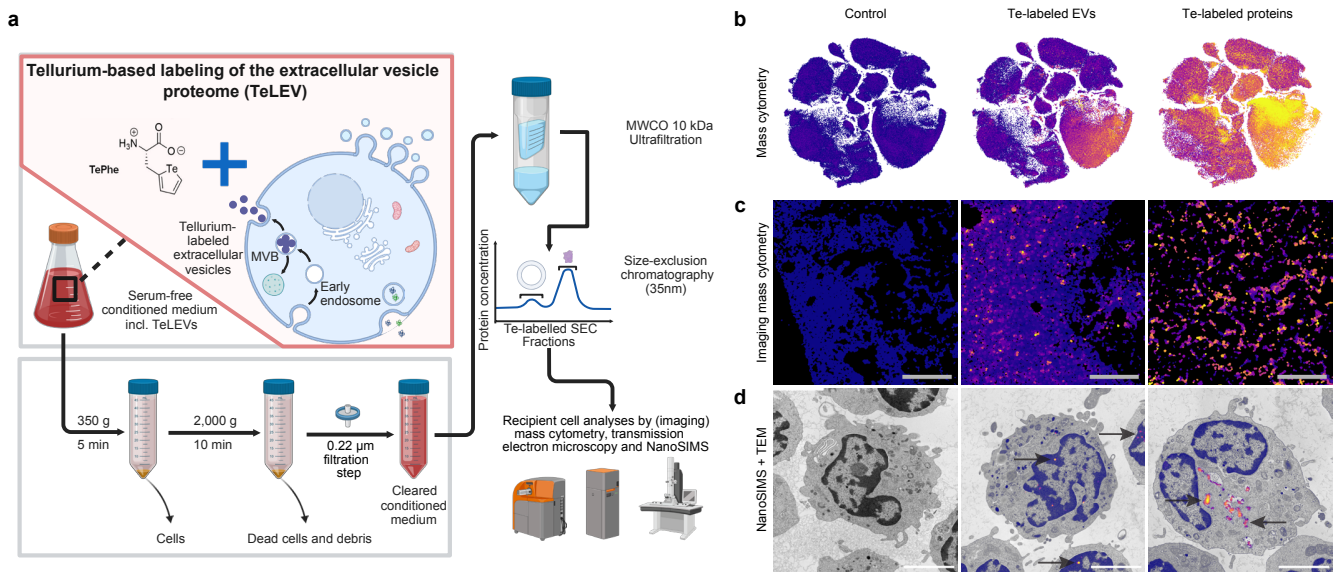
a
Tellurium-based labeling of the extracellular vesicle proteome (TeLEV)
TePhe
Tellurium-labeled extracellular vesicles
MVB
Early endosome
Serum-free conditioned medium incl. TeLEVs
350 g
5 min
2,000 g
10 min
0.22 µm filtration step
Cleared conditioned medium
Cells
Dead cells and debris
MWCO 10 kDa Ultrafiltration
Protein concentration
Size-exclusion chromatography (35nm)
Te-labelled SEC Fractions
Recipient cell analyses by (imaging) mass cytometry, transmission electron microscopy and NanoSIMS
b
Control
Te-labeled EVs
Te-labeled proteins
Mass cytometry
c
Imaging mass cytometry
d
NanoSIMS + TEM

Figure 1

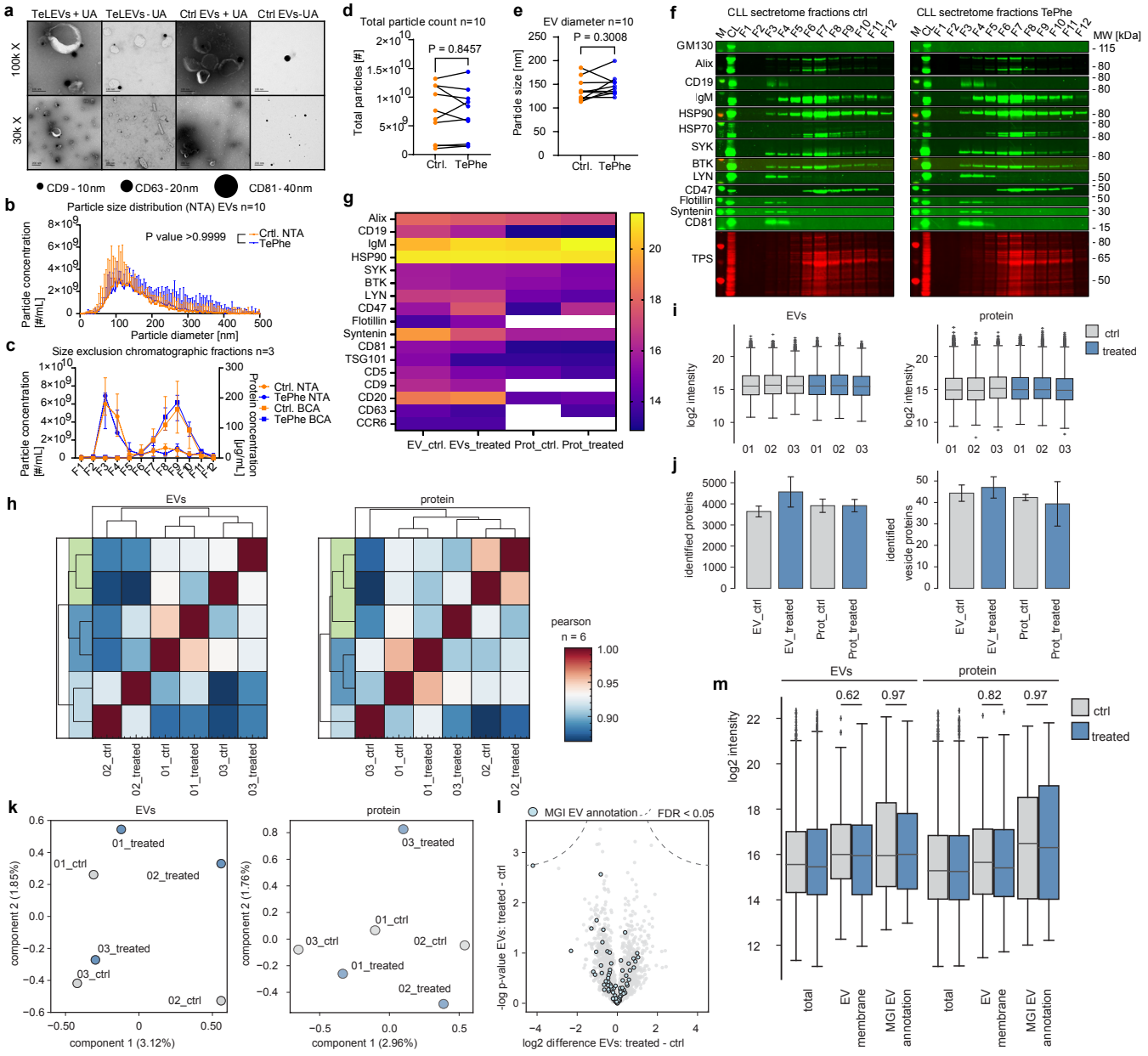
a
TeLEVs + UA
TeLEVs - UA
Ctrl EVs + UA
Ctrl EVs-UA
100k X
30k X
CD9 - 10nm
CD63 - 20nm
CD81 - 40nm
b
Particle size distribution (NTA) EVs n=10
P value >0.9999
Ctrl. NTA
TePhe
Particle concentration [#/mL]
Particle diameter [nm]
c
Size exclusion chromatographic fractions n=3
Ctrl. NTA
TePhe NTA
Ctrl. BCA
TePhe BCA
Particle concentration [#/mL]
Protein concentration [µg/mL]
d
Total particle count n=10
P = 0.8457
Total particles [#]
Ctrl.
TePhe
e
EV diameter n=10
P = 0.3008
Particle size [nm]
Ctrl.
TePhe
f
CLL secretome fractions ctrl
CLL secretome fractions TePhe
MW [kDa]
GM130
Alix
CD19
IgM
HSP90
HSP70
SYK
BTK
LYN
CD47
Flotillin
Syntenin
CD81
TPS
g
Alix
CD19
IgM
HSP90
SYK
BTK
LYN
CD47
Flotillin
Syntenin
CD81
TSG101
CD5
CD9
CD20
CD63
CCR6
EV_ctrl. EVs_treated Prot_ctrl. Prot_treated
i
EVs
protein
log2 intensity
ctrl
treated
j
identified proteins
identified vesicle proteins
EV_ctrl
EV_treated
Prot_ctrl
Prot_treated
h
EVs
protein
pearson
n = 6
02_ctrl
02_treated
01_ctrl
01_treated
03_ctrl
03_treated
k
EVs
protein
component 1 (3.12%)
component 2 (1.85%)
component 1 (2.96%)
component 2 (1.76%)
l
MGI EV annotation
FDR < 0.05
-log p-value EVs: treated - ctrl
log2 difference EVs: treated - ctrl
m
EVs
protein
0.62
0.97
0.82
0.97
ctrl
treated
log2 intensity
total
EV membrane
MGI EV annotation

Figure 2

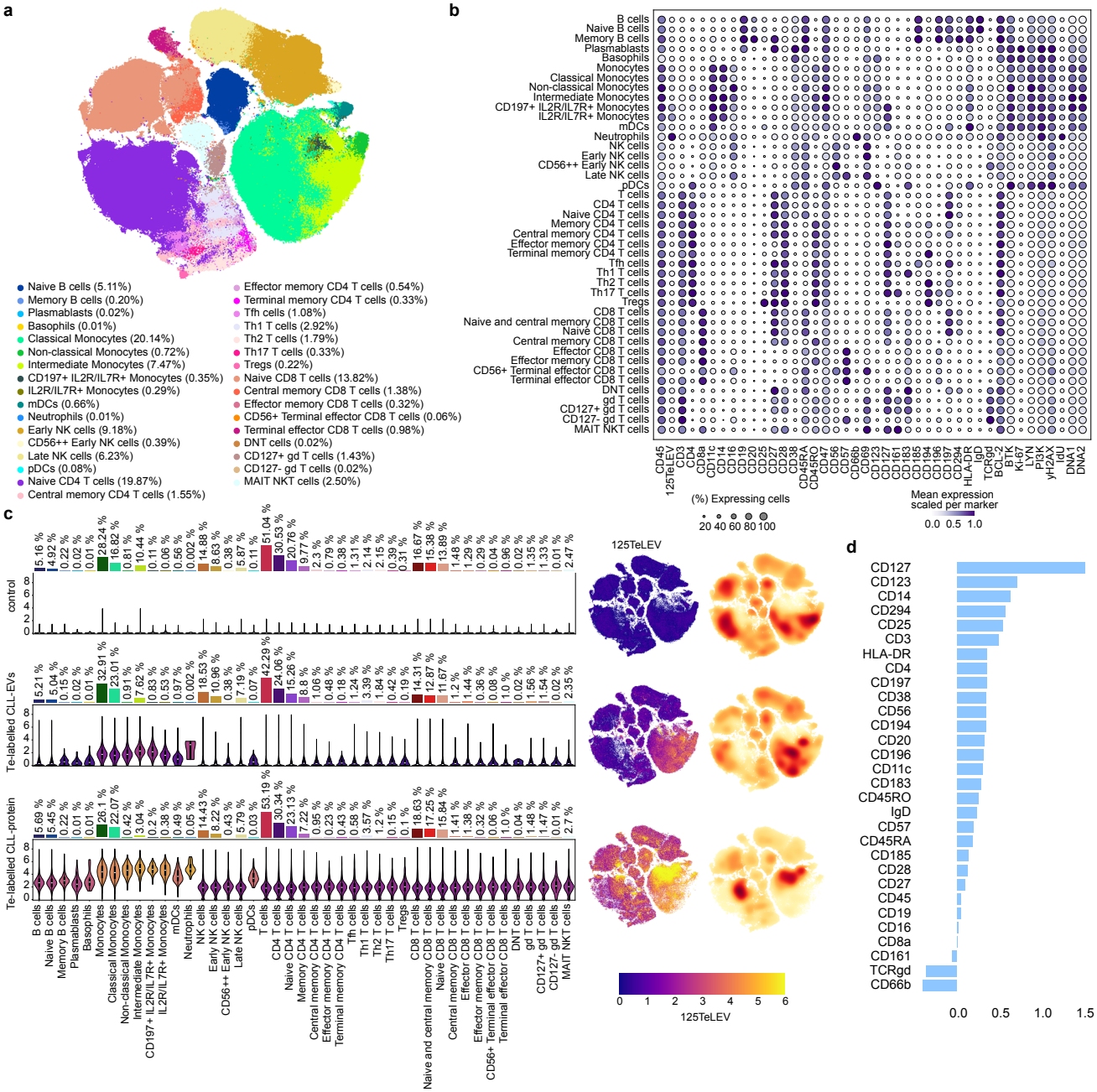
a
Naive B cells (5.11%)
Memory B cells (0.20%)
Plasmablasts (0.02%)
Basophils (0.01%)
Classical Monocytes (20.14%)
Non-classical Monocytes (0.72%)
Intermediate Monocytes (7.47%)
CD197+ IL2R/IL7R+ Monocytes (0.35%)
IL2R/IL7R+ Monocytes (0.29%)
mDCs (0.66%)
Neutrophils (0.01%)
Early NK cells (9.18%)
CD56++ Early NK cells (0.39%)
Late NK cells (6.23%)
pDCs (0.08%)
Naive CD4 T cells (19.87%)
Central memory CD4 T cells (1.55%)
Effector memory CD4 T cells (0.54%)
Terminal memory CD4 T cells (0.33%)
Tfh cells (1.08%)
Th1 T cells (2.92%)
Th2 T cells (1.79%)
Th17 T cells (0.33%)
Tregs (0.22%)
Naive CD8 T cells (13.82%)
Central memory CD8 T cells (1.38%)
Effector memory CD8 T cells (0.32%)
CD56+ Terminal effector CD8 T cells (0.06%)
Terminal effector CD8 T cells (0.98%)
DNT cells (0.02%)
CD127+ gd T cells (1.43%)
CD127- gd T cells (0.02%)
MAIT NKT cells (2.50%)
b
(%) Expressing cells
20 40 60 80 100
Mean expression scaled per marker
0.0 0.5 1.0
c
control
Te-labelled CLL-EVs
Te-labelled CLL-protein
125TeLEV
0 1 2 3 4 5 6
d
CD127
CD123
CD14
CD294
CD25
CD3
HLA-DR
CD4
CD197
CD38
CD56
CD194
CD20
CD196
CD11c
CD183
CD45RO
IgD
CD57
CD45RA
CD185
CD28
CD27
CD45
CD19
CD16
CD8a
CD161
TCRgd
CD66b
0.0 0.5 1.0 1.5

Figure 3

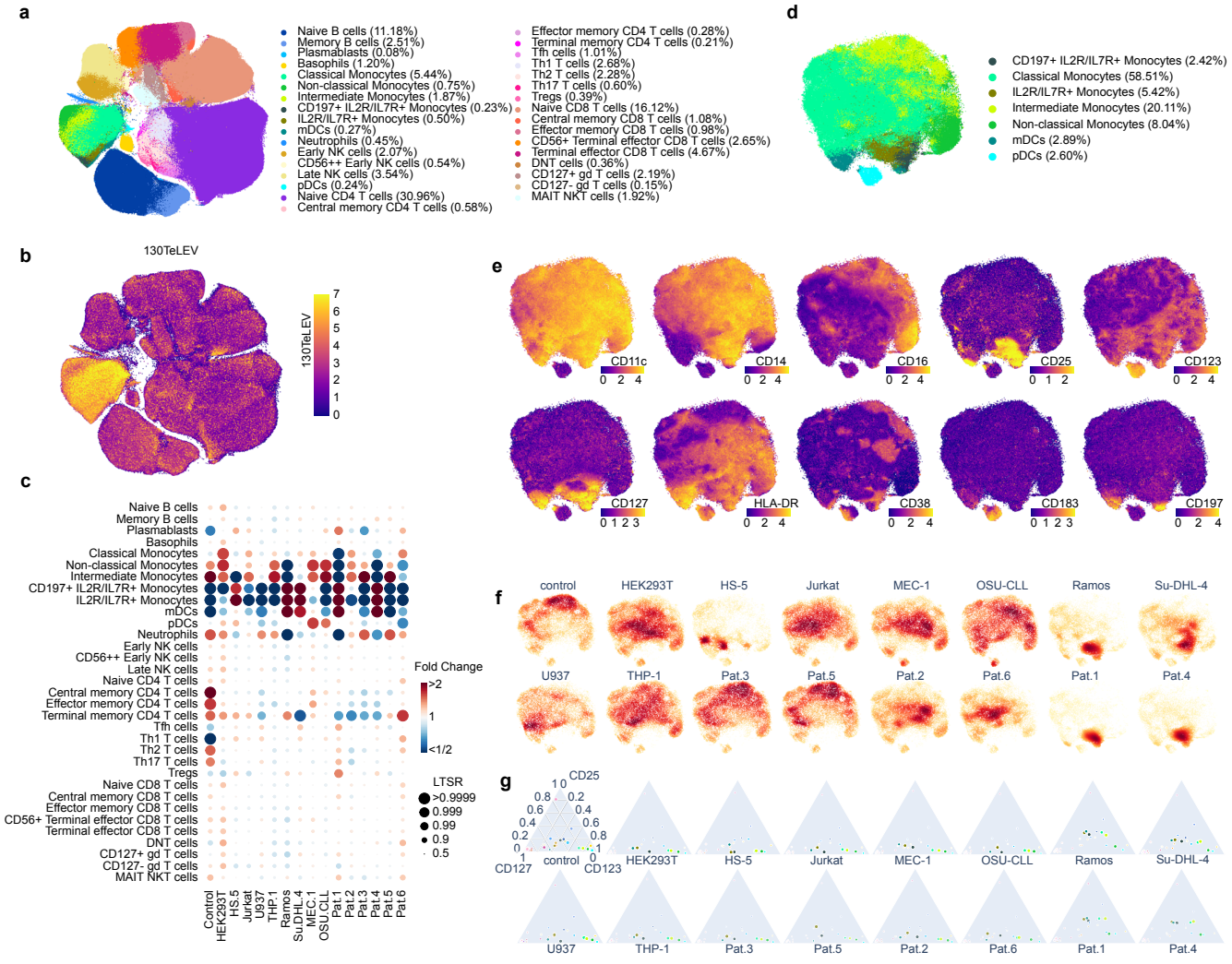
a
Naive B cells (11.18%)
Memory B cells (2.51%)
Plasmablasts (0.08%)
Basophils (1.20%)
Classical Monocytes (5.44%)
Non-classical Monocytes (0.75%)
Intermediate Monocytes (1.87%)
CD197+ IL2R/IL7R+ Monocytes (0.23%)
IL2R/IL7R+ Monocytes (0.50%)
mDCs (0.27%)
Neutrophils (0.45%)
Early NK cells (2.07%)
CD56++ Early NK cells (0.54%)
Late NK cells (3.54%)
pDCs (0.24%)
Naive CD4 T cells (30.96%)
Central memory CD4 T cells (0.58%)
Effector memory CD4 T cells (0.28%)
Terminal memory CD4 T cells (0.21%)
Tfh cells (1.01%)
Th1 T cells (2.68%)
Th2 T cells (2.28%)
Th17 T cells (0.60%)
Tregs (0.39%)
Naive CD8 T cells (16.12%)
Central memory CD8 T cells (1.08%)
Effector memory CD8 T cells (0.98%)
CD56+ Terminal effector CD8 T cells (2.65%)
Terminal effector CD8 T cells (4.67%)
DNT cells (0.36%)
CD127+ gd T cells (2.19%)
CD127- gd T cells (0.15%)
MAIT NKT cells (1.92%)
d
CD197+ IL2R/IL7R+ Monocytes (2.42%)
Classical Monocytes (58.51%)
IL2R/IL7R+ Monocytes (5.42%)
Intermediate Monocytes (20.11%)
Non-classical Monocytes (8.04%)
mDCs (2.89%)
pDCs (2.60%)
b
130TeLEV
130TeLEV
7
6
5
4
3
2
1
0
c
Naive B cells
Memory B cells
Plasmablasts
Basophils
Classical Monocytes
Non-classical Monocytes
Intermediate Monocytes
CD197+ IL2R/IL7R+ Monocytes
IL2R/IL7R+ Monocytes
mDCs
pDCs
Neutrophils
Early NK cells
CD56++ Early NK cells
Late NK cells
Naive CD4 T cells
Central memory CD4 T cells
Effector memory CD4 T cells
Terminal memory CD4 T cells
Tfh cells
Th1 T cells
Th2 T cells
Th17 T cells
Tregs
Naive CD8 T cells
Central memory CD8 T cells
Effector memory CD8 T cells
CD56+ Terminal effector CD8 T cells
Terminal effector CD8 T cells
DNT cells
CD127+ gd T cells
CD127- gd T cells
MAIT NKT cells
Control
HEK293T
HS.5
Jurkat
U937
THP.1
Ramos
Su.DHL.4
MEC.1
OSU.CLL
Pat.1
Pat.2
Pat.3
Pat.4
Pat.5
Pat.6
Fold Change
>2
1
<1/2
LTSR
>0.9999
0.999
0.99
0.9
0.5
e
CD11c
CD14
CD16
CD25
CD123
CD127
HLA-DR
CD38
CD183
CD197
f
control
HEK293T
HS-5
Jurkat
MEC-1
OSU-CLL
Ramos
Su-DHL-4
U937
THP-1
Pat.3
Pat.5
Pat.2
Pat.6
Pat.1
Pat.4
g
CD25
CD127
CD123
control
HEK293T
HS-5
Jurkat
MEC-1
OSU-CLL
Ramos
Su-DHL-4
U937
THP-1
Pat.3
Pat.5
Pat.2
Pat.6
Pat.1
Pat.4

Figure 4

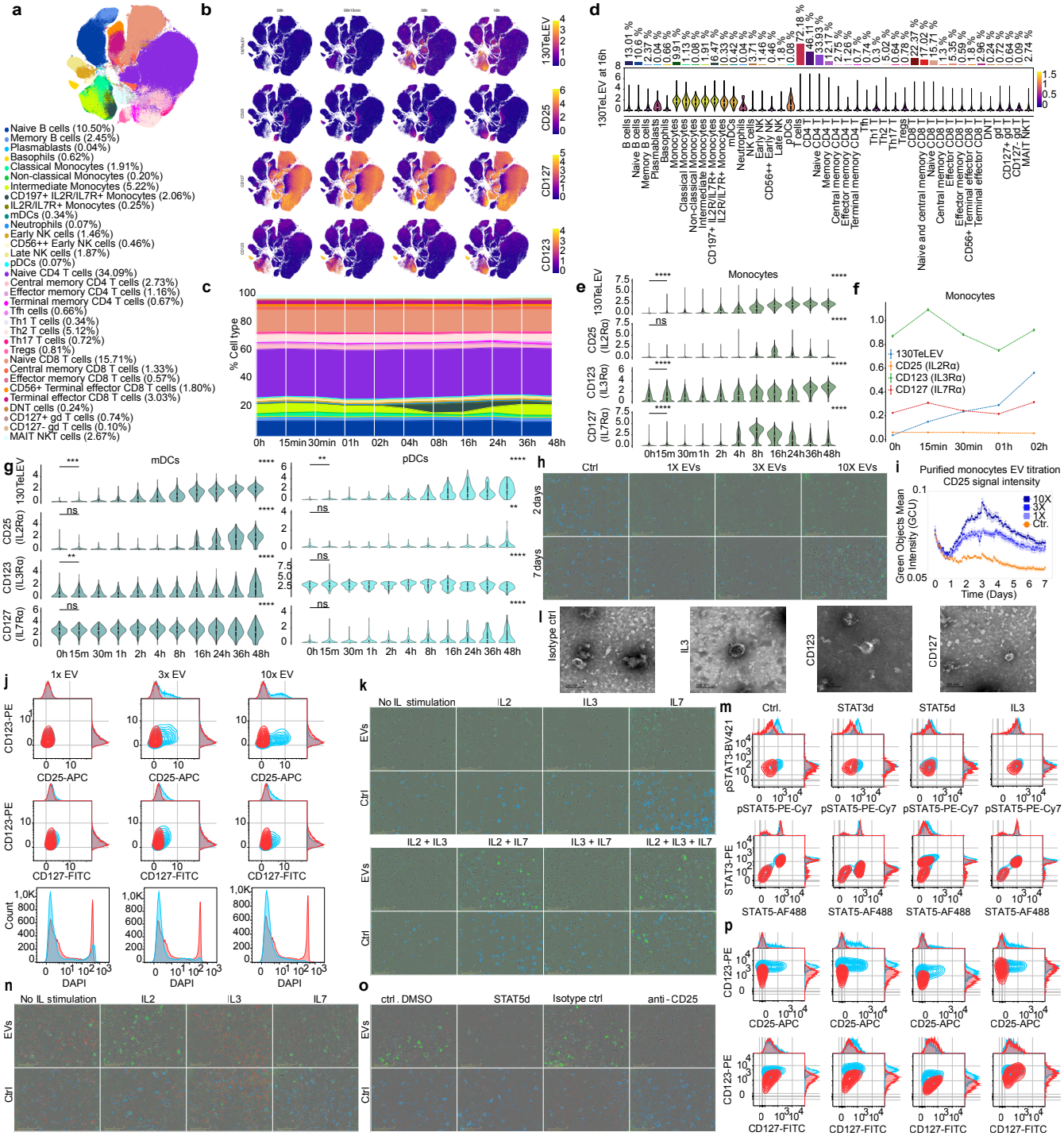
a
Naive B cells (10.50%)
Memory B cells (2.45%)
Plasmablasts (0.04%)
Basophils (0.62%)
Classical Monocytes (1.91%)
Non-classical Monocytes (0.20%)
Intermediate Monocytes (5.22%)
CD197+ IL2R/IL7R+ Monocytes (2.06%)
IL2R/IL7R+ Monocytes (0.25%)
mDCs (0.34%)
Neutrophils (0.07%)
Early NK cells (1.46%)
CD56++ Early NK cells (0.46%)
Late NK cells (1.87%)
pDCs (0.07%)
Naive CD4 T cells (34.09%)
Central memory CD4 T cells (2.73%)
Effector memory CD4 T cells (1.16%)
Terminal memory CD4 T cells (0.67%)
Tfh cells (0.66%)
Th1 T cells (0.34%)
Th2 T cells (5.12%)
Th17 T cells (0.72%)
Tregs (0.81%)
Naive CD8 T cells (15.71%)
Central memory CD8 T cells (1.33%)
Effector memory CD8 T cells (0.57%)
CD56+ Terminal effector CD8 T cells (1.80%)
Terminal effector CD8 T cells (3.03%)
DNT cells (0.24%)
CD127+ gd T cells (0.74%)
CD127- gd T cells (0.10%)
MAIT NKT cells (2.67%)
b
130TeLEV
CD25
CD127
CD123
c
% Cell type
0h 15min 30min 01h 02h 04h 08h 16h 24h 36h 48h
d
130TeLEV at 16h
e
Monocytes
130TeLEV
CD25 (IL2Rα)
CD123 (IL3Rα)
CD127 (IL7Rα)
f
Monocytes
130TeLEV
CD25 (IL2Rα)
CD123 (IL3Rα)
CD127 (IL7Rα)
g
mDCs
pDCs
h
Ctrl
1X EVs
3X EVs
10X EVs
2 days
7 days
i
Purified monocytes EV titration
CD25 signal intensity
Green Objects Mean Intensity (GCU)
Time (Days)
10X
3X
1X
Ctr.
l
Isotype ctrl
IL3
CD123
CD127
j
1x EV
3x EV
10x EV
CD123-PE
CD25-APC
CD127-FITC
Count
DAPI
k
No IL stimulation
IL2
IL3
IL7
IL2 + IL3
IL2 + IL7
IL3 + IL7
IL2 + IL3 + IL7
EVs
Ctrl
m
Ctrl.
STAT3d
STAT5d
IL3
pSTAT3-BV421
pSTAT5-PE-Cy7
STAT3-PE
STAT5-AF488
n
No IL stimulation
IL2
IL3
IL7
EVs
Ctrl
o
ctrl. DMSO
STAT5d
Isotype ctrl
anti-CD25
EVs
Ctrl
p
CD123-PE
CD25-APC
CD127-FITC

Figure 5

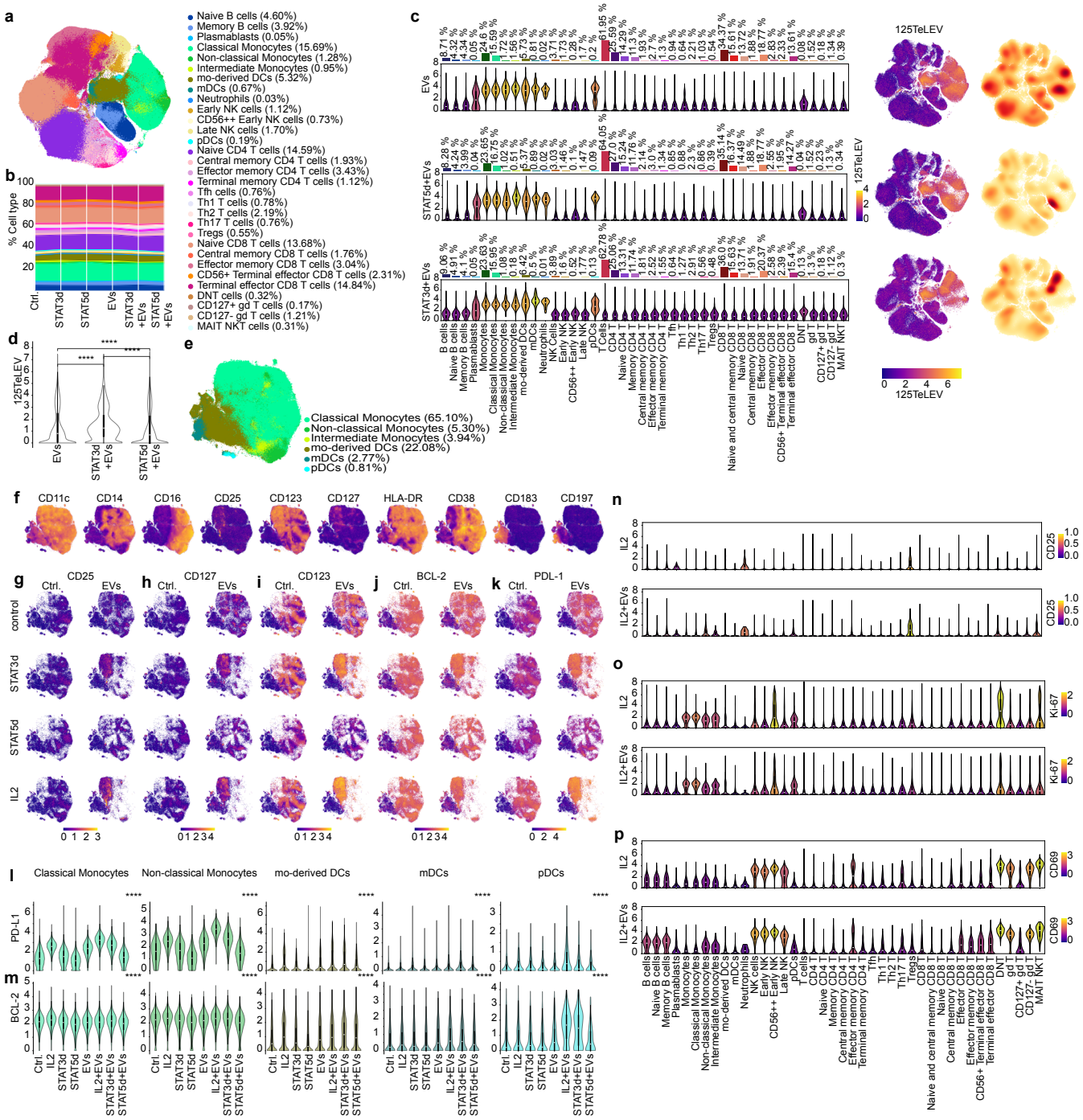
a
Naive B cells (4.60%)
Memory B cells (3.92%)
Plasmablasts (0.05%)
Classical Monocytes (15.69%)
Non-classical Monocytes (1.28%)
Intermediate Monocytes (0.95%)
mo-derived DCs (5.32%)
mDCs (0.67%)
Neutrophils (0.03%)
Early NK cells (1.12%)
CD56++ Early NK cells (0.73%)
Late NK cells (1.70%)
pDCs (0.19%)
Naive CD4 T cells (14.59%)
Central memory CD4 T cells (1.93%)
Effector memory CD4 T cells (3.43%)
Terminal memory CD4 T cells (1.12%)
Tfh cells (0.76%)
Th1 T cells (0.78%)
Th2 T cells (2.19%)
Th17 T cells (0.76%)
Tregs (0.55%)
Naive CD8 T cells (13.68%)
Central memory CD8 T cells (1.76%)
Effector memory CD8 T cells (3.04%)
CD56+ Terminal effector CD8 T cells (2.31%)
Terminal effector CD8 T cells (14.84%)
DNT cells (0.32%)
CD127+ gd T cells (0.17%)
CD127- gd T cells (1.21%)
MAIT NKT cells (0.31%)
b
% Cell type
Ctrl
STAT3d
STAT5d
EVs
STAT3d +EVs
STAT5d +EVs
c
EVs
STAT5d+EVs
STAT3d+EVs
125TeLEV
d
125TeLEV
e
Classical Monocytes (65.10%)
Non-classical Monocytes (5.30%)
Intermediate Monocytes (3.94%)
mo-derived DCs (22.08%)
mDCs (2.77%)
pDCs (0.81%)
f
CD11c
CD14
CD16
CD25
CD123
CD127
HLA-DR
CD38
CD183
CD197
g
CD25
h
CD127
i
CD123
j
BCL-2
k
PDL-1
Ctrl.
EVs
control
STAT3d
STAT5d
IL2
l
Classical Monocytes
Non-classical Monocytes
mo-derived DCs
mDCs
pDCs
PD-L1
m
BCL-2
n
IL2
IL2+EVs
CD25
o
Ki-67
p
CD69

Figure 6